# Multi-instrument observations of soft electron precipitation and its association with magnetospheric flows

Jun Liang,[1] E. Spanswick,[1] M. J. Nicolls,[2] E. F. Donovan,[1] D. Lummerzheim,[3] and W. W. Liu[4,5]

[1] We present a multi-instrument study on the variations of optical auroras and ionospheric electron densities during an interval of a series of fast earthward flows in the magnetotail on 3 March 2009. The flow-related auroral signatures include intermittent higher-latitude (>68° magnetic latitude) intensifications manifested in green and blue line auroras and more latitudinally extended red line auroral intensifications and expansions. During the same interval the Poker Flat incoherent scatter radar (PFISR) detected $F$ region ionospheric electron density enhancements which, together with the red line auroral intensifications, give evidence for soft electron (<1 keV) precipitation associated with fast magnetospheric flow activity. We demonstrated the southward motion of ionospheric electron density patches in correspondence to individual earthward flow bursts and auroral activations. By virtue of the multibeam technique of PFISR we construct the altitudinal profile of the density patches and estimate that the characteristic energies of the precipitating electrons were on order of a few hundred eV, comparable to the observed electron temperature in the near-Earth central plasma sheet (CPS). We propose that the fast flows give rise to enhanced ELF wave activity, which causes strong pitch angle diffusion of the soft electron population in the CPS via wave-particle interactions. The precipitation may be further aided with a moderate field-aligned potential drop comparable to or smaller than the CPS electron temperature. When the flows penetrate into the inner plasma sheet, the adiabatic drift motion of soft electrons may lead to a decreasing trend of electron energy with decreasing radial distance, which is manifested in PFISR observations as an ascending trend of the altitude range of the density patches toward the equatorward auroral border.

## 1. Introduction

[2] Particle precipitation is the dominant source of night-side atmosphere ionization and the associated optical auroral emissions. The altitudinal range where the impact ionization and auroral excitation occur, as well as the "color" (wavelength) of the aurora, is contingent upon the energy spectra of the precipitation particles. In principle, soft electrons (<1 keV) tend to deposit their energy and cause ionizations in the $F$ region ionosphere (altitude >140 km), and con-tribute to the excitation of the red line (630 nm) auroras as one the most visible emissions, while the higher-energy electrons (>1 keV) typically lead to ionization enhancement in the $E$ or $D$ region of the ionosphere, and are responsible for the excitations of, e.g., the green line (557.7 nm) and the $N_2^+$1PG (470.9 nm) auroras. The blue line (427.8 nm) emission tends to be proportional to the total incident energy flux and thus also responds mainly to the energetic electron precipitation. Analysis on the altitudinal profile of the iono-spheric electron density, and the cross-wavelength intensity ratio of the auroral emission can thus be used to estimate the energy spectrum of the incident particles [e.g., *Rees and Luckey*, 1974; *Lummerzheim and Lilensten*, 1994; *Brekke et al.*, 1989; *Semeter and Kamalabadi*, 2005].

[3] Studies on the precipitation-induced ionization/auroral enhancement provide a tool of remote sensing the dynamics of the magnetosphere and the magnetosphere-ionosphere coupling processes. As one of the hottest topics in this regard, the potential auroral signatures of fast flows in the central plasma sheet (CPS) have drawn attention from

---

[1]Department of Physics and Astronomy, University of Calgary, Calgary, Alberta, Canada.
[2]SRI International, Menlo Park, California, USA.
[3]Geophysical Institute, University of Alaska Fairbanks, Fairbanks, Alaska, USA.
[4]Space Science, Canadian Space Agency, Saint-Hubert, Quebec, Canada.
[5]School of Electronic Information, Wuhan University, Wuhan, China.

magnetospheric/ionospheric researchers for decades. In particular, the poleward boundary intensifications (PBIs), including the north–south auroral structures such as "streamers," have been widely considered as the ionospheric manifestations of the fast earthward flows in the midtail plasma sheet [*Henderson et al.*, 1998; *Lyons et al.*, 1999, 2002; *Nakamura et al.*, 2001; *Kauristie et al.*, 2003; *Sergeev et al.*, 2004; *Zesta et al.*, 2000, 2002, 2006; *Liu et al.*, 2008]. The suggested mechanisms linking the magnetospheric flow to the auroral precipitation include the field-aligned current (FACs) along the dusk flankside of the flow channel [e.g., *Nakamura et al.*, 2001; *Sergeev et al.*, 2004], the Alfvenic wave excited at the flow front [*Liu et al.*, 2008] or wavefront propagation of field line resonance at the plasma sheet boundary layer [*Liu et al.*, 1995], and the enhanced wave-particle precipitation in the equatorial CPS [*Kepko et al.*, 2009].

[4] The topic received renewed interests recently with the development of high-resolution, multispectrum imager (MSI) system such as the NORthern Solar Terrestrial Array (NORSTAR). A special class of flow-related auroral signature has been unveiled from NORTSAR measurements. *Kepko et al.* [2009] identified an equatorward moving red line diffuse auroral form ~5 min prior to a substorm onset. Such diffuse auroral forms were not present in the concurrent green and blue line images. During this interval fast earthward flows were observed by THEMIS probes in the near-Earth tail. *Kepko et al.* [2009] suggest that the 630 nm auroral form was created by soft electron precipitation scattered by the earthward flow burst. *Lui et al.* [2010] reported that a red line "streamer" emerging from the diffuse aurora moved westward and poleward, followed by an equatorward retreat. Correspondingly, THEMIS probes detected moderate flows with a vortex pattern compatible with the poleward/equatorward motion of the streamers. To further check the statistical occurrence of red line auroral structures and their association with CPS flows and auroral substorms, a special campaign was conducted using the NORSTAR MultiSpectral Imagers from 18 March to 7 April 2009. Using these data, *Spanswick et al.* [2009] presented many examples of equatorward moving red line auroral structures in the few degrees poleward of auroral brightenings. In some cases, but certainly not all, the arrival of the equatorward moving form at an arc location coincided with an auroral brightening. These auroral "flows" were also shown to be part of a distinct population of features with relatively high equatorward ionospheric speeds. This population exists, as expected, only in the near-midnight region.

[5] The above observations based upon NORSTAR MSI point to the potential linkage between the magnetospheric flows and soft electron precipitation. The absence of corresponding emissions at other wavelengths such as the green and blue lines implies that the characteristic energy of the precipitating electrons is mainly soft. There is however one intrinsic problem with the 630nm auroral measurement that hinders a more quantitative investigation on the precipitation characteristics: the red line aurora can be excited by a broad energy range (a few to a few hundred eV) of precipitating electrons and in turn feature a broad range of emission heights (160–300 km) [e.g., *Meier et al.*, 1989; *Jackel et al.*, 2003], while the ground optical imaging instruments can only measure the integral brightness within a specific line-of-sight bin column. The lack of altitudinal resolution causes difficulties in estimating the precipitation energy spectrum with desirable accuracy, as well as uncertainties in determining the emission latitude, especially for low elevation angle measurements.

[6] The Poker Flat incoherent scatter radar (PFISR) is a new generation of the ISR instrument. Its electronic pulse-to-pulse steering capability allows near-simultaneous measurements of key plasma parameters such as the line-of-sight ion drift velocity, the electron density, the ion and electron temperature in multiple look directions, without physical movement of the radar antenna. The multibeam technique provides the latitude-altitudinal resolution desirable for the study of flow-related precipitation. In particular, a combination of PFISR and optical auroral observations has proven to be a promising research strategy, and provided interesting results and new insights into the nightside auroral ionospheric electrodynamics associated with the PBIs [*Zou et al.*, 2008] and the late growth and expansion phase of the substorms [*Zou et al.*, 2009; *Lyons et al.*, 2010].

[7] In this paper, we will report an event with comprehensive observation data sets from both in situ and ground-based instruments, with particular interest in the soft electron precipitation inferred from the optical auroral and radar measurements and its potential relationship to magnetospheric fast flows. The paper is arranged as follows: In section 2 we shall briefly introduce the instruments involved in this study. Section 3 will detail the observations of fast flows in the tail CPS, optical auroral intensifications at various wavelengths, and the $F$ region electron density patches in conjunction to the flow and auroral activities. In section 4 we shall estimate the characteristic energies of the precipitation electrons from the PFISR measurements, and evaluate possible underlying mechanisms associating the CPS flow enhancement with the soft electron precipitation. Section 5 provides further discussions on the flow-related precipitation in the inner plasma sheet. Section 6 concludes the paper.

## 2. Instruments

[8] The PFISR at Poker Flat (65.13° N, −147.47° W Geo.) is one of the three faces (two more being built in Resolute Bay, Canada) of the Advanced Modular Incoherent Scatter Radar (AMISR). During the event interval PFISR was run in the Aurora and Convection mode, which consisted of 13 beam directions. Figure 1a shows the elevation angles and the azimuths of the beams, and Figure 1b shows the AACGM projection of the beams. Among the 13 beams, beam 12,10,9, and 13 are magnetic north pointing but in ascending order of elevation angles. Beams 4, 3, 2, and 1 are northwest directed, while beams 8, 7, 6, and 5 are northeast directed. These two sets of beams are roughly symmetric with respect to the radar magnetic meridian. Beam 11 is designed as magnetic-field-aligned. The beam widths are between 1 and 1.5°.

[9] In normal operation mode two types of pulses were transmitted, a long pulse (480 $\mu$s) and an alternating code pulse (30 $\mu$s). The two pulse modes were designed as the standard $F$ region experiment and $E$ region experiment, respectively. Since the primary parameter of this paper's interest is the electron density $N_e$, we shall introduce our
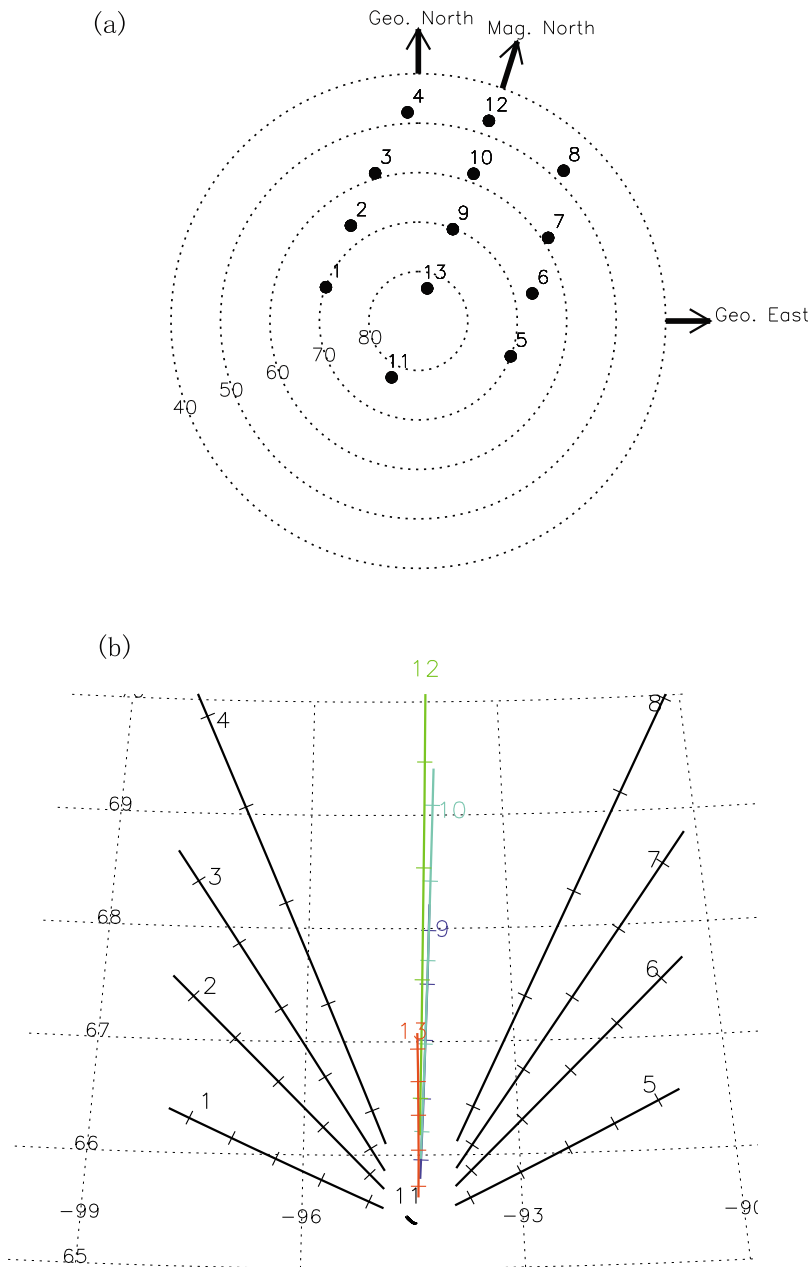
**Figure 1.** (a) Elevation angles and azimuths of the PFISR beams. The center circle denotes the radar location, and the numbered circles indicate the elevation angles. (b) AACGM projection of the beams. The short dashes across the beam lines indicate where the beam altitudes are 100, 200, 300, 400, and 500 km, from short to long beam range.

procedures in retrieving $N_e$ from raw observational data sets. Under the Bunemen approximation [*Evans*, 1969], $N_e$ is proportional to the received backscattered power as

$$P_r = \frac{G_{sys}}{r^2} \cdot \frac{N_e}{(1 + k^2\lambda_D^2)(1 + k^2\lambda_D^2 + T_e/T_i)}, \quad (1)$$

where $k = 4\pi/\lambda_0$ is the Bragg wave number for backscattering; $\lambda_0$ is the radar wavelength; $\lambda_d$ is the electron Debye length; $T_e$ and $T_i$ are the electron and ion temperature, respectively; $r$ is the range; $G_{sys}$ is a system constant containing the transmit power and the antenna gain correction.

In practice, the ambiguity of $N_e$ determination mainly comes from the uncertainty in the electron-to-ion temperature ratio. The raw received power is designed to be oversampled with range separation of ~4.5 km. This resolution is of course often degraded by the range smearing effect. Based upon the raw backscattered power measurement a so-called "uncorrected $N_e$" is calculated from (1) on the assumption of $k\lambda_D \rightarrow 0$ and $T_e = T_i$, which might be applicable in the $E$ region but is definitely problematic in the $F$ region, particularly during auroral precipitation intervals [e.g., *Semeter and Kamalabadi*, 2005].

[10] In the standard PFISR data processing routine, for both the long-pulse and alternating code pulse modes the autocorrelation functions (ACF) of the received signal are fitted according to the plasma wave theory of incoherent scatterers [*Evans*, 1969; *Waldteufel*, 1971]. The data provider (M. Nicholls) developed an iterative approach to obtain the best fit parameters such as the ion composition, electron and ion temperatures from the ACF. The integral range for such ACF fit procedure is ~36 km for long-pulse mode and ~9 km for alternating code mode. Such fitting is of course not always successful, and at times yields problematic data points. The large errors and/or failures of the ACF fit may result from a variety of reasons, e.g., the inapplicability of the theoretical model to the actual scatter physics, inappropriately determined or specified ion compositions, or low signal-to-noise ratios. Consequently, the outcomes of such ACF fit procedure often appear to be somewhat "scrappy", as one may notice from the left side of Figure 10 later. The potential inaccuracy of the ACF fit procedure can usually be inferred from the large error estimates of the fitting parameters involved.

[11] Since the $N_e$ enhancement of our interest in this study was mainly observed in the ionospheric $F$ region, the long-pulse mode data are preferentially used. Recommended by the data provider, an innovative algorithm was developed to combine the advantages of the "uncorrected $N_e$" data set and the ACF-fit data set. We first perform a weighted least squares polynomial regression to the ACF-fit $T_e$ and $T_i$; the standard errors of $T_e$ and $T_i$ inherited from the ACF-fit data set are used as the weight factors of the regression: the smaller the error of a data point, the larger its weight in the regression. The polynomial regression is performed in sliding widows: three-point linear in $E$ region or five-point cubic in $F$ region. The procedure acts to "smooth out" those ACF-fit $T_e$ and $T_i$ data with large errors and/or noise spikes. Based upon the polynomial regression, $T_e$ and $T_i$ are recalculated at the ranges where the "uncorrected $N_e$", or equivalently the raw backscattered power, are sampled; the "corrected $N_e$" is then obtained from equation (1) and becomes the final data outcome to be used throughout this paper. The above procedure yields a proper compromise between the range resolution and the noise reduction of the long-pulse mode data, and is found suitable for the interest of this study. Meanwhile, the ACF-fit $N_e$ data in alternating code pulse mode are also presented in this paper, mainly for the purpose of a qualitative comparison with the $N_e$ profile from the above depicted approach based upon long-pulse mode data.

[12] The other key instrument involved in this study is the multichannel meridian scanning photometer, also at Poker Flat (PFMSP). Four auroral emission lines are monitored, the red line (630 nm), the green line (557.7 nm), the blue line (427.8 nm), and the proton $H_\beta$ line (486.1 nm), with time resolution of 15s. The scan lines are inside the magnetic meridian and thus facilitate a coordinated comparison with the PFISR observations on its magnetic northward pointing beams, though the PFMSP meridian conforms to the 1983 epoch of magnetic north pole and thus has a slight deviation from the PFISR magnetic meridian. Optical auroral measurements were also taken from THEMIS white light all-sky imagers (ASIs) [*Mende et al.*, 2008] at Fort Yukon (FYKN) with 3s cadence. The white light imager has

an effective band pass of 400–700 nm, and by nature contains a mixture of visible emission lines such as green and red line auroras, which are originated at different altitudes.

[13] THEMIS [*Angelopoulos*, 2008] probes provide the in situ measurements of the event. The onboard instruments used in this study include the Fluxgate Magnetometer (FGM) [see *Auster et al.*, 2008], the Electrostatic Analyzer (ESA) [see *McFadden et al.*, 2008], the Solid-State Telescope (SST), and the Electric Field Instrument (EFI) [see *Bonnell et al.*, 2008]. The FGM instrument measures the in situ magnetic field with accuracy of 0.01 nT. The data used in this study are in spin resolution (~3 s). The ESA instrument measures the flux of thermal particles over the energy range from 5 eV to 25 keV for ions, and 6 eV to 30 keV for electrons. The ESA is the key instrument in this study since it provides the ion flow velocity and electron temperature most relevant to our research interest. The SST measures the energy flux of superthermal (>30 keV) particles from specific directions. The EFI provides electric field measurements in three independent directions. To infer the plasma waves in the extremely low frequency (ELF) range two spectral data sets are involved: the FilterBank (FBK) and fast Fourier transform (FFT). The FBK data set has continuous time coverage but poor spectral resolution with only 6 frequency bands. The FFT data set contains 64 frequency bins but is only available during particle burst mode intervals. For detailed description of the FBK and FFT data sets as well as a complete list of their frequency bins and band widths see *Cully et al.* [2008].

## 3.  Observations

### 3.1.  Context and Observation Geometry of the Event

[14] The event of interest occurred during 10–12 UT on 3 March 2009. Inferred from the OMNIWeb solar wind data (not shown) shifted to the bow shock nose, the IMF $B_z$ was dominantly positive during 8–14 UT, with a few southward excursions at ~0935, ~1020, and ~1040 UT. The IMF $B_y$ was exclusively positive. There might be a causal relationship between those IMF $B_z$ southward excursions and the midtail flow enhancements (to be reported below) with proper time lags [*Nakamura et al.*, 1999], but a pursuit of this link is not the objective of this research. Inferred from available ground magnetometer and auroral observations there was no substorm activity in 2 h prior to the event; the THEMIS AE index was below 80 nT from 0830 UT till throughout the event. As we shall illustrate later, although the fast flows gave rise to pronounced auroral activities, they were not followed by a substorm expansion.

[15] The observation geometry of the event is assembled in Figure 2. Figure 2a gives the GSM X-Y positions of the five THEMIS probes, and Figure 2b shows their ionospheric projections based upon the T96 model with average IMF parameters inferred from the OMNIWEB data. The field of view (FOV) of the FYKN ASI, the PFISR beam geometry, and the sites of ground magnetometers involved in this study are also plotted for reference. The local magnetic midnight of FYKN and PF both occur at ~11 UT, such that our observations were confined within ±1h MLT around midnight.

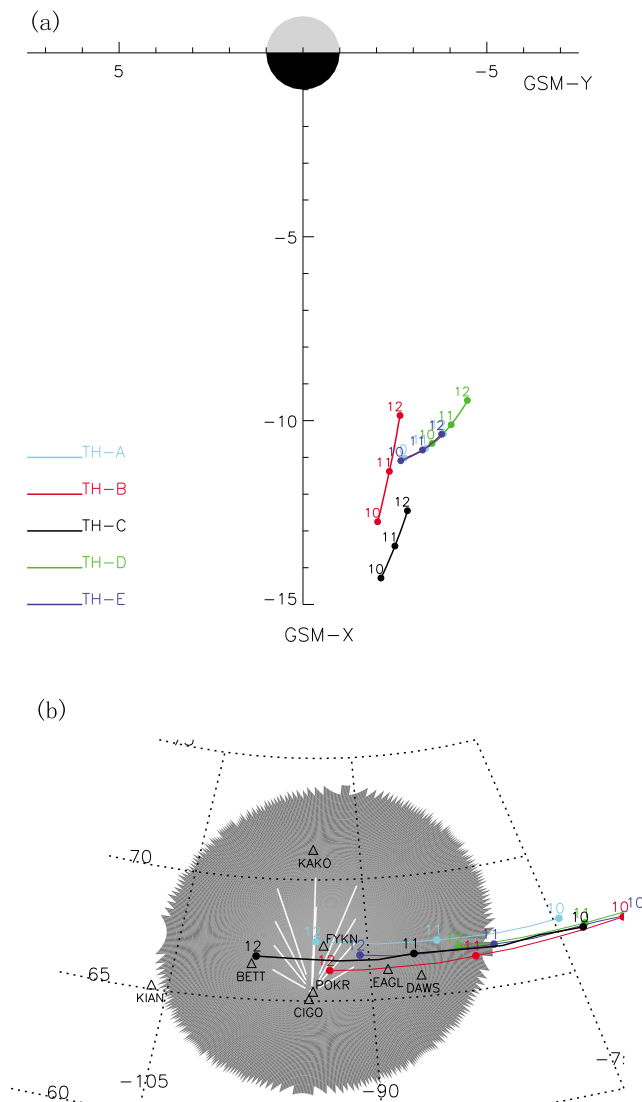[16] Since this study contains rather comprehensive observations and complicated analyses, to avoid baffling the

**Figure 2.** (a) GSM X-Y positions of five THEMIS probes during 1000–1200 UT. (b) Their ionospheric projections based upon the T96 model. The FOVs of the FYKN ASI are shown in the gray circle, and the PFISR beams are shown by white lines. The magnetometer sites involved in this study are shown by triangles. The map grid is in AACGM coordinates.

readers we provide at the end of the manuscript a schematic chart (Figure 16) which threads all the key observations and our proposed scenarios, including their places in this paper and relevant figures. The chart may greatly facilitate one to read through the paper.

### 3.2. THEMIS In Situ Observations

[17] Among the five THEMIS probes TH-C was located in a key transition region (X = −13 to −14 Re) between the midtail and the inner plasma sheet, and mapped closest to the FOV of the ASI and radar, though admittedly the probe was up to ~1 h MLT east to the radar FOV at the start of the event. Figure 3 shows the magnetic and plasma observations from TH-C. From top to bottom are the magnetic fields in

GSM coordinates, ion flow velocities in GSM, ion number density, ion and electron temperatures, plasma $\beta$, and the omnidirectional energy flux spectrogram of electrons, respectively. The high-energy (>30 keV) particle fluxes measured by the SST are involved in the calculation of the plasma moments such as the number density, temperature and the pressure, but their contributions are found small only. During ~1025 UT to ~1120 UT TH-C detected a series of fast earthward flows, with typical characteristics of the "busty bulk flows" (BBFs) [e.g., *Angelopolous et al.*, 1994; *Cao et al.*, 2006]. The first flow burst around ~1030 UT was moderate in magnitude (~200 km/s), while the probe was likely off the equatorial plasma sheet by then inferred from the relatively low $\beta$ values. All the other flow bursts were rather strong, reaching ~600 km/s for the two strongest flow burst intervals around ~1100 and ~1116 UT.

[18] Figure 3 (bottom), e.g., the electron energy flux spectrogram, combines the ESA (6 eV to 30 keV) and SST (>30 keV) measurements. Despite the strong flow disturbance there was no clue of electron injection, i.e., a significant enhancement in energetic (> > 1 keV) electron flux. Taking into account the fact that for a Maxwellian distribution the energy flux maximizes at $2T$ in which $T$ is the temperature, we infer that the electron temperature $T_e$, albeit some moderate increase accompanying the flow enhancement, stayed below 1 keV during the entire event interval, which can be confirmed in the fifth panel of Figure 3. Therefore in terms of the number fluxes, which maximize at $T_e$, the soft electrons dominated. Admittedly, due to the dynamic magnetic field variations TH-C alternated between the CPS and the plasma sheet boundary layer (PSBL) during the event interval, inferred from the fluctuation of plasma $\beta$ above and below one, such that the observed variations of energy flux contained a mixture of temporal and spatial effects.

[19] Figure 4a gives the FBK wave data of TH-C EFI. Despite the low spectral resolution (only 6 frequency bands) of the FBK data set it is interesting to note that there were broadband wave intensifications in the ELF range accompanying each individual flow bursts. Such ELF wave intensifications were marginally discernible for the first flow burst interval when the probe was located at the PSBL and the flow magnitude was moderate, but were rather pronounced for other flow bursts. During two major flow burst intervals, 1055–1105 UT and 1113–1120 UT, the TH-C EFI was run in particle burst mode and yielded the FFT data set, which contains 64 frequency channels. Figure 4b shows the FFT spectrogram from the measurements on the spin plane sensor EDC34 for the above two intervals. For reference we overplot the electron gyrofrequency $f_{ce}$ according to the local magnetic field measurements. It is clear that the broadband ELF wave intensification extend well to and even above the $f_{ce}$. In a company study (J. Liang, manuscript in preparation, 2011) we perform an extensive survey on fast flow events in the midtail CPS from THEMIS observations, and statistically confirmed that it is a common scenario that ELF waves over broad frequency range intensify with the fast earthward flows. During the particle burst mode intervals the THEMIS probe is occasionally run in wave burst mode, which only has a duration of 8 s but in this brief interval full raw data sample (8192/s) of three-dimensional electric and magnetic field data are saved. Using these data
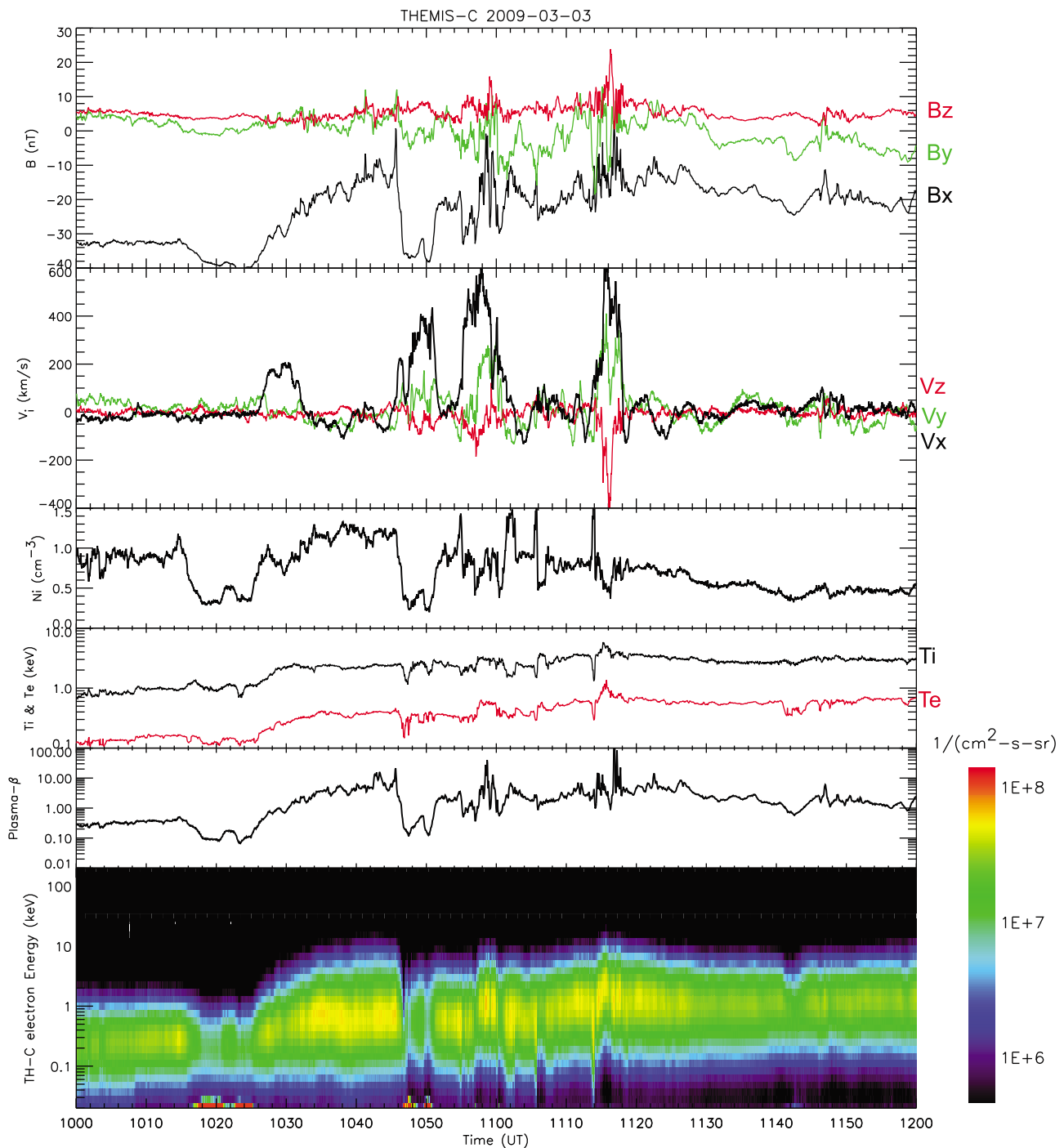
**Figure 3.** From top to bottom: the magnetic fields in GSM (X is shown in black, Y is shown in green, and Z is shown in red for the first two panels), ion flow velocities in GSM, ion number density, average ion (black) and electron (red) temperatures, plasma $\beta$, and the omnidirectional energy flux spectrogram of electrons observed on TH-C.

we exemplify in Figure 4c the wave power spectra of $E_{DSL\_x}$ and $B_{DSL\_z}$, in Despun Sun L-vectorZ (DSL) coordinates, for a whistler wave burst centered at ~1100:02 UT. Note that in this snapshot example, embedded in a broadband turbulence-like spectrum both electric and magnetic waves feature a narrowband maximum at f~0.7 $f_{ce}$ as well. We have actually performed further polarization analysis (not shown) and confirmed that such narrowband wave structure

does represent a whistler mode. This piece of observation in Figure 4c is to be used to support the demonstration of the whistler cyclotron resonance in section 4.2 later.

[20] As shown in Figure 2, TH-B was roughly radially aligned with TH-C but about 2 $R_E$ inward. Figure 5, in the same format as Figure 3, gives the observations on TH-B. We see that the flows were largely reduced in magnitude, and appeared as wave-like oscillations around zero, consistent
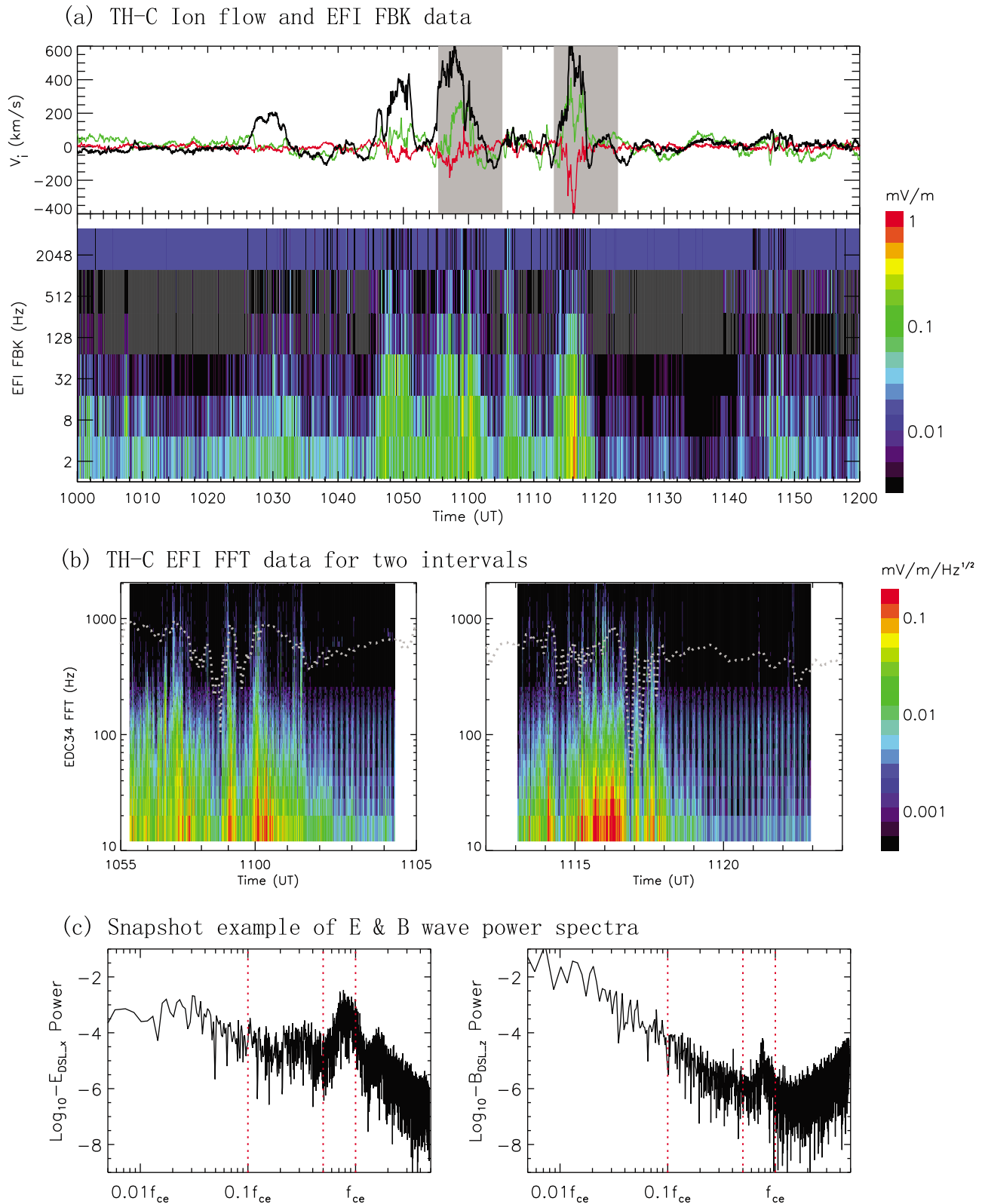
**Figure 4.** (a) FBK data of TH-C EFI. The ion flow velocity is also plotted to facilitate a comparison. Two gray bands mark the intervals of particle burst mode. (b) FFT data of the TH-C EDC34 sensor for two particle burst mode intervals. The local electron gyrofrequency $f_{ce}$ is plotted as dashed lines for reference. (c) A snapshot example of the wave power spectra of (left) $E_{DSL\_x}$ and (right) $B_{DSL\_z}$ calculated from EFI and search coil magnetometer wave burst mode measurements, respectively, at ~1100 UT.
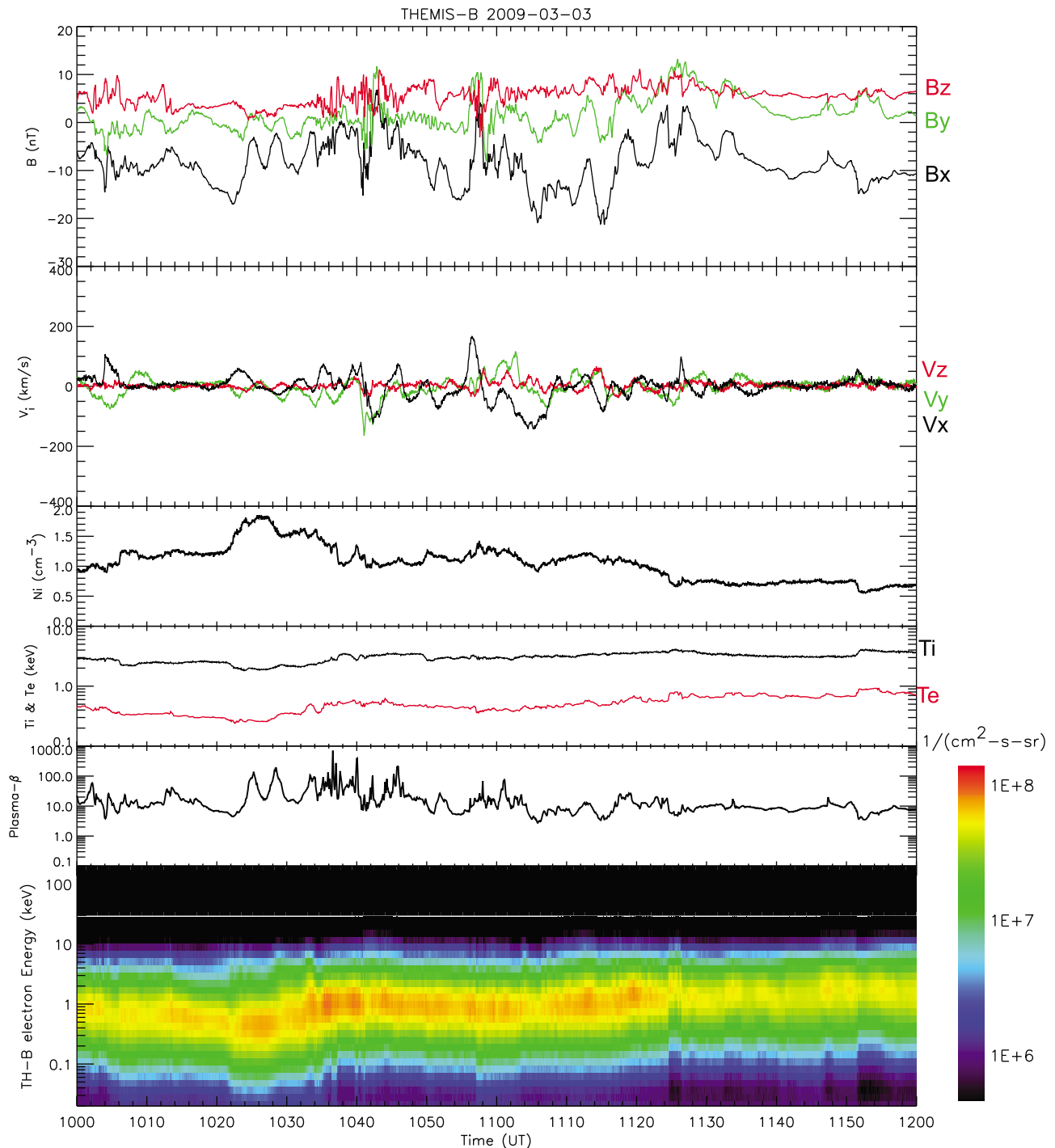
**Figure 5.** TH-B observations in the same format as Figure 3.

with the notion that when BBFs penetrate and "brake" in the inner CPS they turn into in a vortical pattern with interleaving earthward and tailward flows [*Panov et al.*, 2010]. During the event interval TH-B remained close to the neutral sheet, as can be inferred from the large plasma–$\beta$ ($\geq$10) and substantial $B_z$ component. This geometry enables us to investigate the temporal variation of the electron flux at the equatorial CPS, without much complication by spatial effects as contained in TH-C observations. As we may see from Figure 5 (bottom),

though there was moderate enhancement of the energy flux during 1025 to 1125 UT, which roughly coincident with the fast flow interval observed on TH-C, the CPS electrons were not much energized; $T_e$ remained below 1 keV during the entire event interval. Combining the particle observations on TH-C and TH-B we conclude that, despite the strong flow activities the ambient CPS electrons stayed essentially soft, with temperature of a few hundred eV. This observation will be key to our understanding of the origin and mechanism of
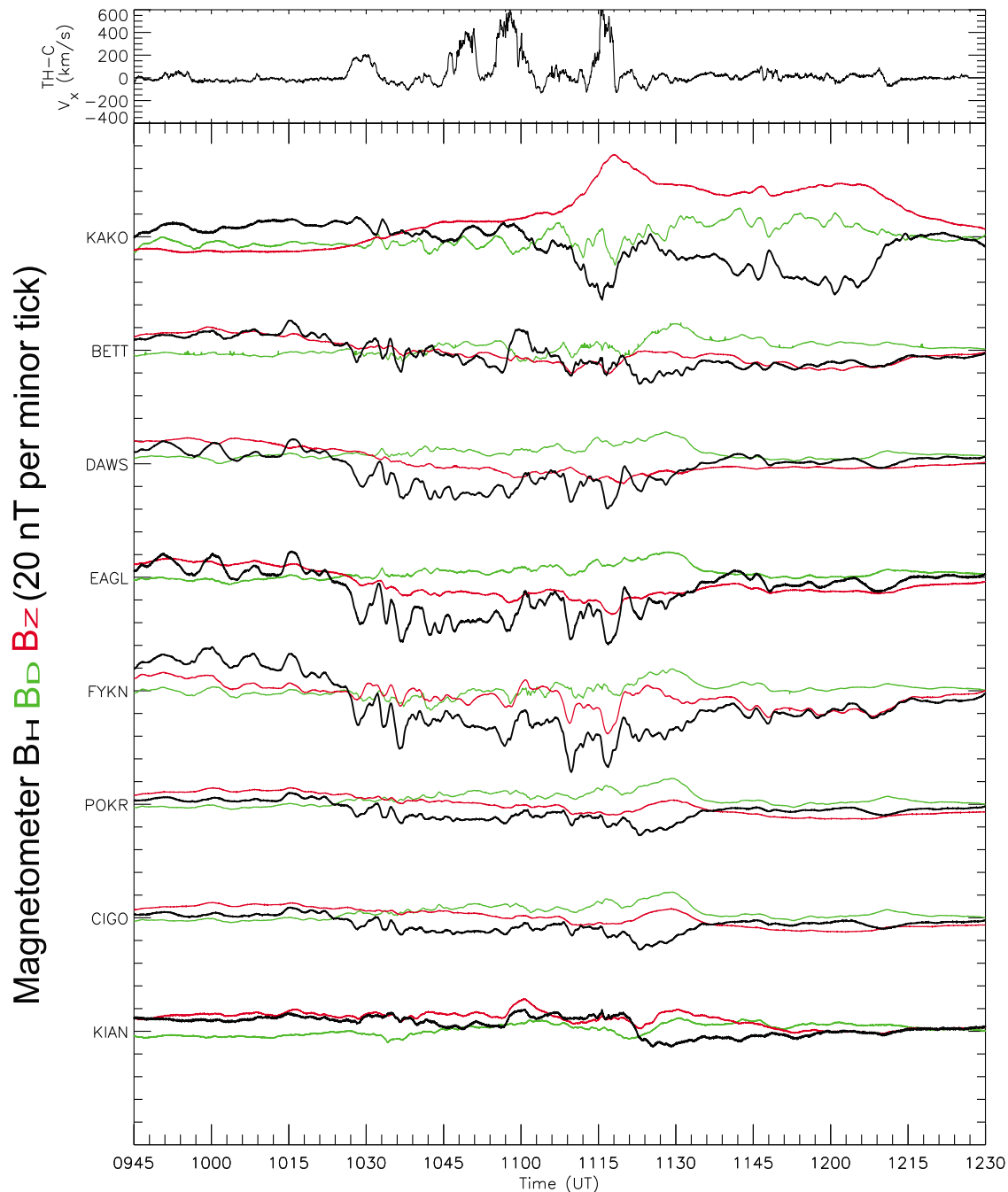
**Figure 6.** (top) Reproduction of the TH-C flow $V_x$ observation for reference. (bottom) The magnetometer data from the GIMA array and the Dawson station. Black, green, and red lines denote the $H$, $D$, and $Z$ components of the magnetic field. The scale is 20 nT per tick such that the stations are separated by 100 nT.

the soft electron precipitation inferred from optical and radar measurements.

[21] The other three THEMIS probes, TH-A, D, and E were further inward and east of TH-C and B, and mapped east of the radar and ASI FOV, We shall not present their observations in this paper, but their summary plots are readily available from the official THEMIS website. We summarize two main features of their observations relevant to the research interest in this paper. (1) Similar to TH-B, TH-E and D detected oscillating flow perturbations with

weak amplitude. TH-A detected some strong flows but at different times from those on TH-C. The observations give implication that that the flows might exist in form of multiple narrow channels, and were sharply braked, probably in a oscillatory fashion [*Panov et al.*, 2010], when penetrating into the inner plasma sheet. (2) None of the three probes (among them TH-D was also close to neutral sheet) revealed noticeable high-energy electron injection signature; their observed $T_e$ were always below 1 keV during the entire event interval. Note that though the probes were located east
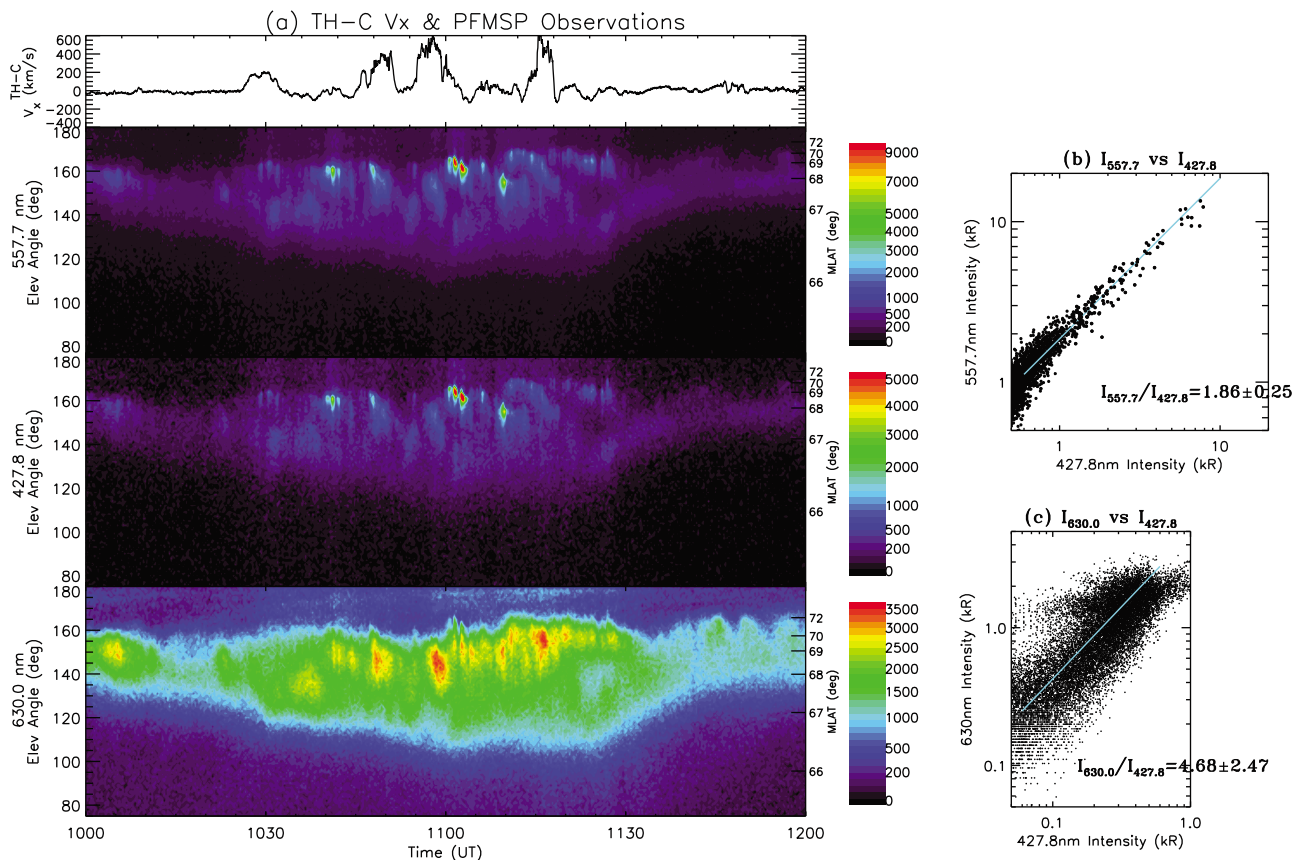
**Figure 7.** (a) Reproduction of the TH-C flow $V_x$ observation for reference and the green line, blue line, and red line emissions measured by PFMSP. The left-hand Y ticks of each PFMSP panel indicate the elevation angle (0°S, 180°N), while the right-hand Y ticks denote the AACGM latitude by assuming a 110 km emission height for green line, blue line, and proton auroras and 200 km for the red line auroras. (b) Scatterplot of green line emission intensity versus the blue line intensity. The colored line indicates a constant ratio of 1.86 between them. (c) Scatterplot of red line emission intensity versus the blue line intensity at latitudes <68° MLAT. The colored line indicates a constant ratio of 4.68 between them.

of the observation sector of our core interest, they still helped to confirm the absence of high-energy electron injection in our interested sector because, had the latter really occurred it should have also been observed by the eastern probes as well, due to the expected eastward drift of high-energy electrons.

### 3.3. Ground-Based Magnetic and Optical Auroral Observations

[22] Figure 6 gives the ground magnetometer observation from GIMA chain and Dawson station of CGSM chain (see Figure 2 for magnetometer locations). We see that roughly corresponding to the TH-C fast earthward flow interval (~1025–1125 UT), there were moderate magnetic disturbances on order of a few tens of nT. These disturbances did not resemble typical negative magnetic bays characteristic of a substorm expansion, but more notably featured ULF oscillations in Pc5–Pc6 frequency range, which were found often accompanying the PBI activities [*Lyons et al.*, 2002].

[23] Figure 7a presents the PFMSP auroral observations. We reproduce the $V_x$ flow component from TH-C observation on the top of Figure 7a for reference. The remainder

of Figure 7a gives the intensities of green line, the blue line, and the red line emissions. We have assumed an emission height of 110 km for the first two emission lines and 200 km for the red line auroras [*Jackel et al.*, 2003]. There were a few intermittent bright "spots" of green and blue line emissions near the poleward edge of the MSP FOV. Those bright "spots" also have their correspondences in the 2-D auroral measurements from THEMIS ASI, which will be presented later. In our following presentation we nominally classify such higher-latitude activities as "PBI", with a caveat that their exact nature might be somewhat questionable since the poleward boundary of the auroral oval could not be accurately estimated from available observations. This ambiguity however would not affect the main research interest of the paper, since we focus more on the auroral activities at lower latitudes than those "PBIs". As can be seen from Figure 7a, at latitudes below those PBIs the overall intensities of the green and blue line auroras was fairly weak, at most a few hundred Rayleigh. The red line auroras, on the other hand, show a different pattern. While there were also several "patchy" intensification structures in the poleward potion of the FOV (>68° magnetic latitude (MLAT)), the overall red line auroral brightness was more

diffusive, ranging between 1 and 2.5 kR, at lower latitudes <68° MLAT. Aside from the intensification in brightness there was also noticeable expansion of red line auroras after ~1025 UT, marked by a southward extension of the equatorward auroral border from ~67° to 66° MLAT. Such motion stalled at ~1100 UT, and then retreated poleward and faded after ~1125 UT. The interval of the intensification and expansion of the auroras is coincident with the overall fast flow interval observed by TH-C.

[24] The intensity ratio between different auroral emission wavelengths may convey important information of the precipitation energy spectrum. In particular, since the green line emissions are responsive to energetic electron precipitation, while the blue line auroras are approximately proportional to the total energy flux, and since the two emissions can be reasonably assumed to originate from the same emission height, the green-to-blue ratio would yield a measure of the average energy of the incident energetic electrons [e.g., *Rees and Luckey*, 1974; *Steele and McEwen*, 1990]. For this purpose we sample the green line auroral intensities and the blue line intensities measured at the same time and same elevation angle, and present their scatterplot in Figure 7b. We see that the green-to-blue ratio is clustered around a constant ratio (1.86 ± 0.25) for the blue line intensities ≥1 kR. Such property can also be directly inferred from Figure 7a in that those green and blue line bright "spots" are very alike in appearance. Based upon this near-constant green-to-blue ratio we estimate that they were contributed by ~5 keV monoenergetic electron precipitation [*Rees and Luckey*, 1974]. At latitudes below those bright "spots," the blue line intensity was low and the red line auroras dominated as revealed in Figure 7a. Inferring the average electron energy from red-to-blue intensity ratio is subject to more ambiguity than that from green-to-blue ratio, partly due to the uncertainty of the emission height of the red line auroras. Figure 7c presents the scatterplot of the intensity of the red line auroras and the blue line auroras at latitudes <68° MLAT. The points were sampled at the same time and the same latitude by assuming a 110 km and 200 km emission height for the blue and red line auroras, respectively. From Figure 7c we see that, though the distributions are a little bit more scattered, the red line auroral intensity is a few times larger than the blue line intensity, with an average ratio of ~4.7. Referring to the observations by *Steele and McEwen* [1990] and the simulations by *Rees and Luckey* [1974], we infer that the electron characteristic energy $E_0$ in the region ~66–68° MLAT would be on order of a few hundred eV.

[25] Figure 8 shows a few cropped frames of the auroral images from the THEMIS white light ASI at FYKN. We have purposefully chosen the intervals that could be reasonably, within the propagational uncertainties of a few minutes, attributed to individual flow bursts detected by TH-C. Readers are referred to the supplementary auroral Movie 1 in 3 s cadence during the entire event interval. The white light imager has no discrimination on the "colors" of the auroral emission, such that its observation contains a mixture of emissions from visible wavelengths. The AACGM coordinates shown in Figure 8 (and the MLAT contour shown in Movie 1) are based upon the assumption of 110 km emission height, which is appropriate for the green and blue line emissions but certainly inaccurate for the red line. We outline two salient features inferred from the ASI observation as follows.

[26] 1. Conformal to the PFMSP green and blue line observations, the overall auroral activities were characterized by intermittent PBIs, which in general originated at latitudes >68° MLAT from the western portion of the ASI FOV (and thus west of the radar FOV), and subsequently showed pronounced eastward expansion across the ASI FOV. They manifested in a variety of auroral forms; they might be arc-like, ray-like, or swirl-like. Many of such PBIs stayed at >68° MLAT during their life time. Some of those higher-latitude intensifications did propagate southward, but they often rapidly faded in luminosity at lower latitude, and were accompanied by a reintensification at latitudes >68° MLAT.

[27] 2. Minutes after the beginning of each PBI there was often brightening of an equatorward arc along ~67° MLAT. Such equatorward arc was distinctly separated from the PBI. None of the equatorward arc intensifications subsequently evolved into a substorm breakup. Instead, they faded away when their leading high-latitude intensification was over.

[28] Though it is very likely that the observed auroral activities were related to fast flows in the tail, a detailed one-to-one correlation between them appears to be complicated. We particularly note that, while every individual flow burst can be rather unambiguously linked to a PBI activity, some of the latter seem to be without appreciable counterparts in in situ flows. For example, during 1037–1042 UT there was prominent auroral intensification at >68° MLAT viewed from THEMIS ASI, but without evidence of fast flow from concurrent TH-C observation. Also, after 1120 UT the in situ flows became rather quiet yet there were still some remnant auroral activities. This discrepancy should not be surprising. The in situ detection of the fast flows is well known to be heavily contingent upon the probe location. In short, fast flows are confined in flow channels with finite Y (azimuthal) and Z (distance to neutral sheet) dimensions, and tend to be decelerated in near tail [e.g., *Nakamura et al.*, 2004; *Miyashita et al.*, 2000]. In our observation geometry the PBIs always originate from the westside of the ASI FOV, while TH-C was located in the eastern portion of the FOV. Also, TH-C was located at X > −14 Re and kept moving earthward during the event interval. It is thus understandable that some of the fast flow activities that led to the auroral intensifications might not be detectable on TH-C.

## 3.4. PFISR Observations

[29] We first briefly survey the ionospheric convection pattern during the event interval. Figure 9 gives the VLOS (line-of-sight velocity) profiles from four PFISR beams 4, 12, 8 and 7. All VLOS measurements are adjusted according to the magnetic aspect angles, i.e., the angle between the beam direction and the magnetic field, such that the velocities shown in Figure 9 represent the flow component in the plane of beam direction and geomagnetic field, and perpendicular to the latter (field-aligned flows are ignored). Beam 12 is a magnetic north directed beam such that it measures purely meridional flows. The beam 12 observations clearly reveal the emergence of strong southward flows over the latitudinal range 67–68° MLAT between 1025 and 1125 UT, while before and after this time interval weaker poleward flows prevail. Beams 4 and 8 are tilted to
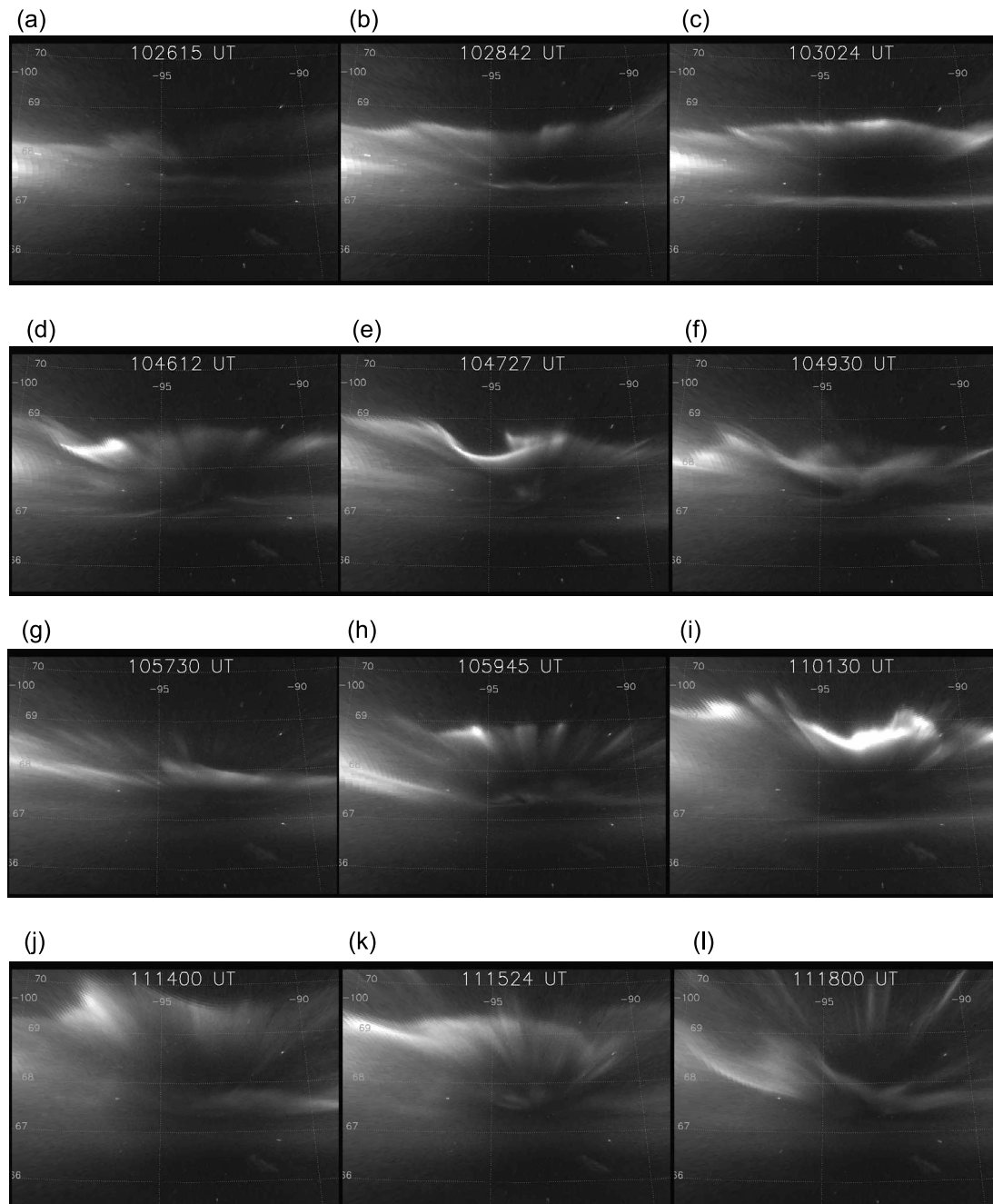
**Figure 8.** Selected frames of FYKN ASI observations. The images are cropped to center around the radar FOV.

west and east of the radar magnetic meridian, respectively, such that their VLOS measurements contain partial contributions from zonal flow component. The VLOS observation on beam 4 is fairly similar to that on beam 12 but reveals even stronger toward radar flows between 1025 and 1125 UT. The observations on beam 4 and 12 confirm that during the fast earthward flow intervals in the tail there were correspondent enhancements of ionospheric southward flows, though their causal relationship would be complicated by a number of factors, e.g., the relative geometry among the flow region, the satellite, and the radar FOV, as well as uncertainties in the M-I coupling process such

as the Alfvenic transit time and ionospheric conductance. These ionospheric southward flows range between 200 and 600 m/s, and show a general trend of decreasing magnitude toward lower latitudes. The VLOS pattern on the eastside beam 8 however, is noticeably different, featuring a mixture of toward radar and away from radar flows. The observations can be explained by the presence of substantial eastward flow component, which is consistent with the sense of propagation of the PBIs inferred from the THEMIS ASI observations. Such eastward flows would enhance the toward radar component on westside beam 4 but reduce that on eastside beam 8. To further verify the existence of eastward
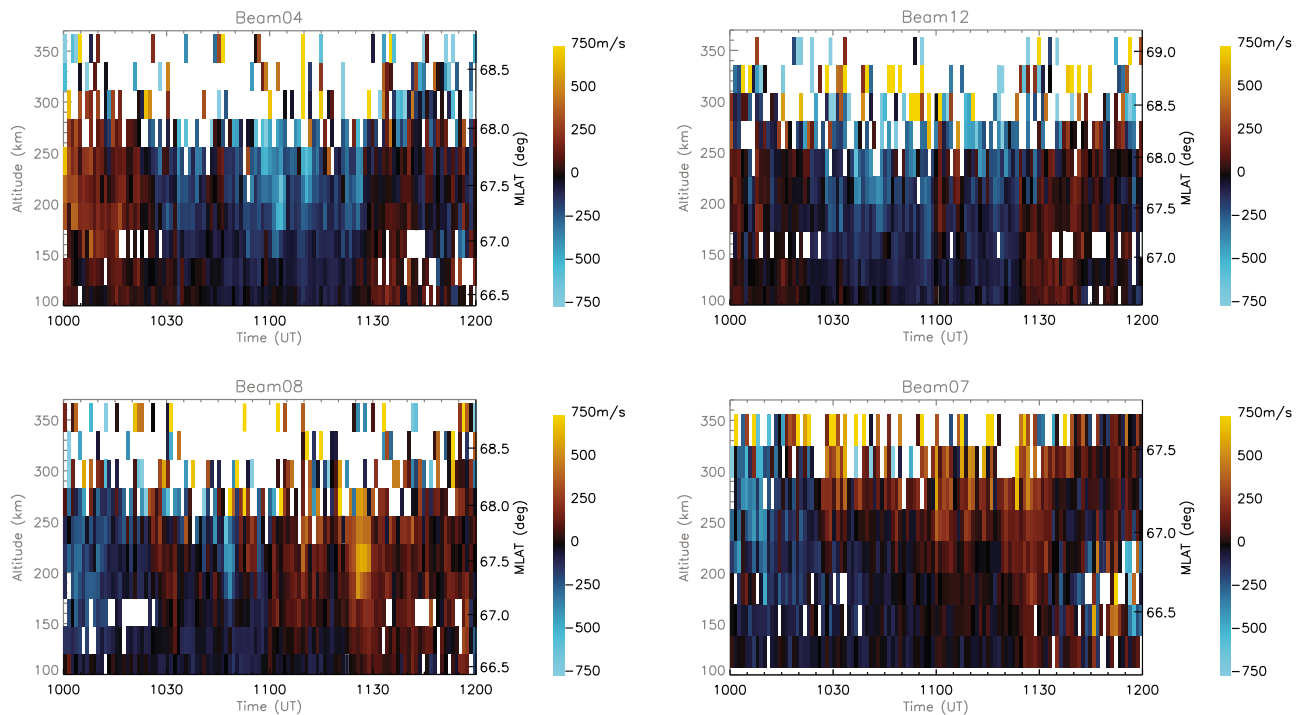
**Figure 9.** ACF-fit VLOS measurements from PFISR beams 4, 12, 8, and 7. Positive value indicates the away from radar component, while negative value indicates the toward radar component. Data with standard error larger than the ACF-fit VLOS itself are ignored and left as white blanks occasionally seen in the plot.

flow component we also present the VLOS measurements along beam 7, whose pointing is even more tilted to eastward than beam 8. Beam 7 observation shows that substantial away from radar flow component first emerges at the higher latitudes (>67.5° MLAT) after ~1025 UT. Such eastward flows is also seen at lower latitudes (<67° MLAT) but lags in appearance. Combining the above VLOS observations we are able to depict the overall ionospheric convection pattern during the interval of interest: the ionospheric flows were in general southeastward, and in particular, east of the radar meridian the flows became strongly eastward. Furthermore, the flows gradually penetrated to lower latitudes with decreasing magnitude.

[30] The PFISR-measured electron density ($N_e$) profiles constitute a vital part of observations in this study. Figure 10 gives the temporal evolution and altitudinal/latitudinal distribution of $N_e$ on four magnetic meridian beams, 12, 10, 9, 13, obtained from the alternating code and long-pulse modes, respectively. Note that for the alternating code pulse we have used the original ACF-fit data of this mode, while for the long-pulse mode data, we have applied addition procedures, as described in detail in section 2, to "smooth out" potentially wrongly estimated ACF-fit data points. In short, the two data sets presented in Figure 10 are based upon different observational modes and independent data processing procedures; it is thus understandable that their results are not without difference. However, they yield fairly compatible patterns of temporal variation and spatial distribution. We shall outline the following salient features from the $N_e$ observations in both modes, with comparison to

the concurrent and colocated PFMSP red line auroral observations.

[31] 1. All beams detect noticeable enhancements of $N_e$ during the event interval of interest, 1025–1130 UT. The intensifications were strongest, and apparently "patchy," on the most oblique (which in turn measuring the most poleward latitudes) beam 12. The density enhancements were dominantly observed in the $F$ region ionosphere on all beams. This can be better verified when we check the alternating code pulse data, which have altitudinal resolution of ~6 km (beam 12) to ~9 km (beam 13), suitable for the $E$ region. Though the data seem a little bit fragmentary due to the reason mentioned in section 2, none of the beams revealed systematic $N_e$ enhancement at altitudes <130 km. However, we caution here that our measurement of the altitudinal $N_e$ distribution might be subject to some uncertainties due to the limitation of beam geometry, an issue we hall address when we introduce the MLAT altitude slices of multibeam observations (see Figure 12) later in section 3.4.

[32] 2. Observations on oblique beams consistently show a southward expansion of the density structure till ~1100 UT; the motion then stalled for a while and retreat northward after ~1130 UT. This motion pattern is in full accordance with that of the red line auroras observed by PFMSP. Understandably such southward/northward motion is not well seen on beam 13 which is near vertical.

[33] 3. The density enhancements gradually lag in appearance time, weaken in magnitude, and increase in altitudes on beams with successively higher-elevation angles. Since higher-elevation angle beam by nature measures
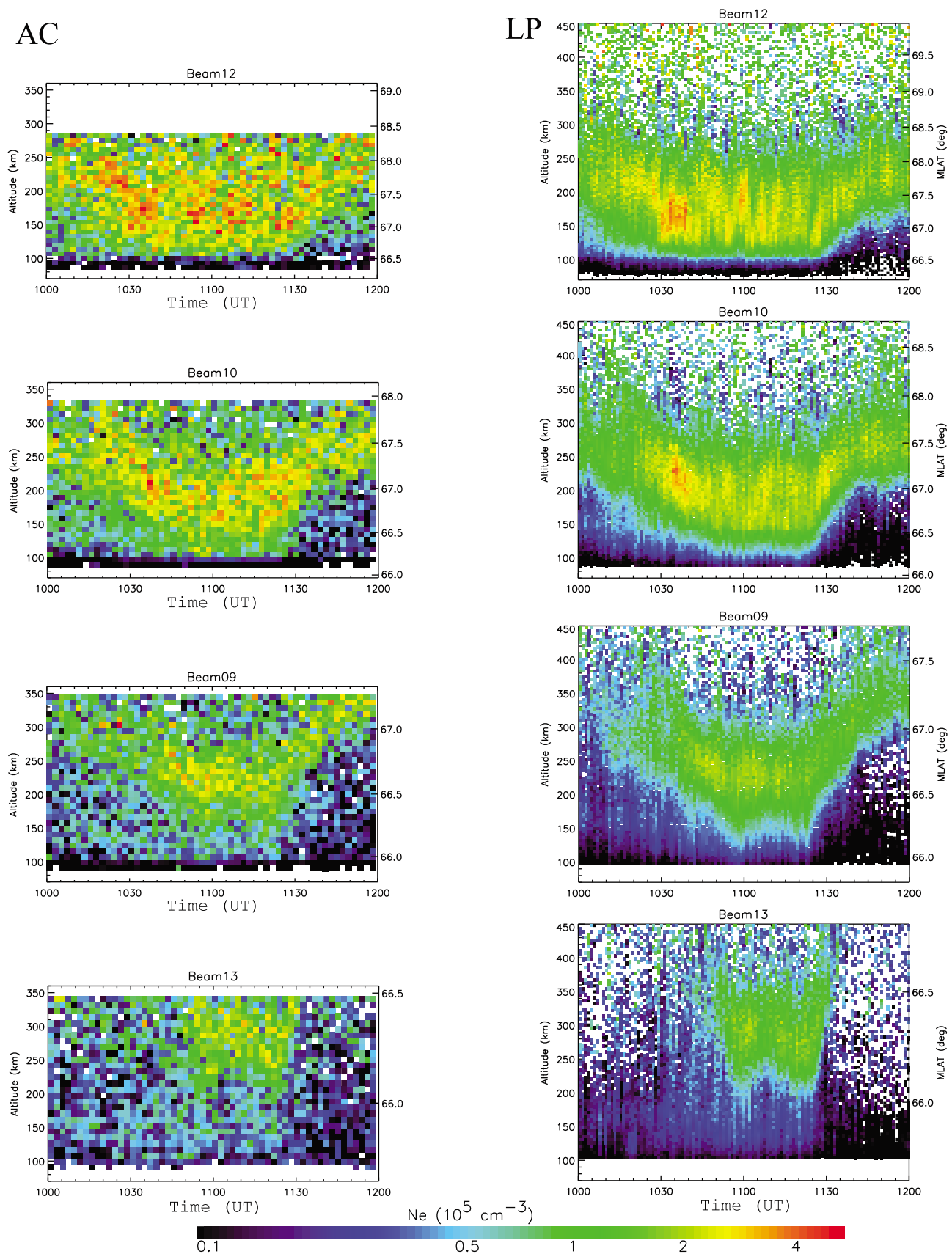
**Figure 10.** Temporal evolution and altitudinal-latitudinal distribution of $N_e$ on four magnetic meridian beams (12, 10, 9, and 13) from (left) alternating code and (right) long-pulse mode measurements. In each panel the left-hand Y ticks denote the altitude, while the right-hand ticks denote the AACGM latitude.

lower latitudes, the lag in the appearance time of the density enhancement is simply another manifestation of the southward motion of the auroras. The implication of the ascending altitudinal range of density enhancements with decreasing latitudes will be discussed in section 4.

[34] Figure 11 presents the $N_e$ measurements in long-pulse mode on all 13 beams. The panels for each beam are arranged roughly according to actual beam geometry (see Figure 1b), north to south from top to bottom and west to east from left to right. In the middle column the first four panels simply repeat those in Figure 10; the beam 11 panel represents the most equatorward (65.4 MALT) beam of PFISR. The backscattered echoes were lacking on this beam due to low electron density, implying that the beam was located south of the auroral region. It is important to note that the above summarized features for the meridional beams are also evident on both the westside beam group and eastside beam group, e.g., strong patchy intensifications on the most poleward beams, southward expansion and then later northward retreat of the density structures, ascending altitudinal levels of the density enhancement with decreasing latitudes, etc. The above observations hint that the longitudinal extension of the density enhancement region is comparable to or even larger than that of the radar FOV. There is however, one noteworthy east–west asymmetry: though beam 1 and 5 are essentially symmetric with respect to the radar meridian, and measure roughly the same latitudes (~66° MLAT), the density patch is well discernible on east beam 5 but not so on west beam 1.

[35] The observations from the poleward PFISR beams (e.g., see beams 4, 8, and 12 in Figure 10), and from the poleward potion of the PFMSP red line auroras (Figure 6, bottom), both reveal that there were a number of discrete, "patchy" intensifications structures. Those patches appeared as near-vertical and/or slightly slanted traces in a MLAT time plot. In the following we shall demonstrate the frame-by-frame evolutions, in MLAT altitude slices, of the PFISR density patches during two example intervals, 1025–1031 UT and 1058–1103 UT, in conjunction with the concurrent in situ flow bursts and PBIs. The integration time of the PFISR data is about 1 min; the label on top of each frame marks the center time of the integration. One should note that since the ionization enhancement contains an integral effect (see equation (2) later) while the auroral emission is more or less a prompt reaction to the precipitation, the two phenomena are not necessarily synchronous in terms of the intensification, though their general tendencies of variation should be comparable.

[36] Figure 12a presents the interval corresponding to the ~1030 UT flow burst in the tail, which is also the start of the whole event. Strong density patch emerged at 200–250 km altitude, 67.5–68° MLAT at ~1026 UT, which is also roughly the start time of the in situ fast flow and the auroral activity (Figure 8a). In the following minutes, the density enhancement extended progressively southward, while the auroral intensification from ASI observation essentially maintained above 68° MLAT, though there were transient and rapidly decaying arcs moving toward lower latitude (Figure 8b). By ~1030 UT the density patch had reached ~67° MLAT and showed no more noticeable southward motion. Meanwhile, an equatorward arc, also at ~67° MLAT (Figure 8c), began to brighten.

[37] Figure 12b shows the interval corresponding to the ~1100 UT flow burst. The in situ fast flow actually started at ~1055 UT and there were some weaker auroral activations before 1058 UT (Figure 8g) that led to moderate density enhancements. However, those preexisting electron density enhancements are found to relax on the 1058 UT frame, presumably due to the recombination. We shall focus on the new generation of density patches associated with the more pronounced and longer-lasting PBI activation at ~69° MLAT after 1159 UT (Figure 8h). The overall sequences are fairly similar to those in previous interval in terms of both the optical and radar observations, with differences in a few subtleties. Noticeable density patch was first seen from PFISR observations between 67.5 and 67.9° MLAT at ~1059 UT. In the following minutes the density patch appeared to migrate toward lower latitudes. Eventually the density patch settled at 66.8–67.2° MLAT at ~1102 UT. Also, an equatorward arc gradually appeared and intensified at ~67° MLAT after ~1101 UT (Figure 8i).

[38] Admittedly, due to the geometry limit there was no lower-altitude observation for oblique beams at long ranges, such that the altitudinal distribution of the density patches are unobtainable at those beam ranges. The PFISR was thus not geometrically favorable to detect the density enhancement directly related to the PBIs at >68° MLAT. However, the PFISR observations nevertheless unveiled noticeable density enhancement in the $F$ region ionosphere, together with the PFMSP measurements that red line auroras dominated at latitudes below those PBIs, the optical and radar observations would to say the least suggest that a substantial portion of the precipitation spectra were composed of soft electrons. More importantly, the altitudinal coverage of PFISR is improved at shorter beam ranges. On a careful look at the final panels of Figures 12a and 12b one can notice that, when the southward moving density patches had anchored at ~67° MLAT, the peak enhancement was *not* observed at the lowest measurable altitudes but unambiguously at heights >140 km. To better illustrate this point, as well as to prepare for a quantitative estimation of the characteristic energy and precipitation flux of the incident electrons in section 4, we present in Figures 13a and 13b the altitudinal $N_e$ profile sampled from PFISR observations for the two flow intervals in Figures 12a and 12b. The sampling is made on all beams within ±0.25° around 67° MLAT, and ±2° within the radar meridian (−94.4° MLON). In Figure 13 the open circles denote the preflow measurements at (Figure 13a) 1025 UT and (Figure 13b) 1058 UT, while the solid circles denote the measurements (Figure 13a) 1031 UT and (Figure 13b) 1102 UT, when the density patch had grown at ~67° MLAT. The data in Figure 13 thus approximately yield the altitudinal profile of the density enhancement at ~67° MLAT, as a consequence of individual earthward flow bursts in the tail. Albeit a little bit scatter in data due to a number of reasons, it is clear that the strongest enhancements take place at an altitudinal range of about 150–180 km, with peak increment around $1.5$–$2 \times 10^5$ cm$^{-3}$. The peak ionization height is slightly higher for interval Figure 13a than for interval Figure 13b. Above 200 km height the density increments become much less noticeable. We note that the density patch investigated in the above examples represents somehow the high end of the observed $N_e$ enhancement; the overall PFISR $N_e$ magnitude is in

**Figure 11.** Temporal evolution and altitudinal-latitudinal distribution of $N_e$ on all PFISR beams from long-pulse measurements. The panels for each beam are arranged roughly according to actual beam geometry, north to south from top to bottom and west to east from left to right. In each panel the left-hand Y ticks denote the altitude, while the right-hand ticks denote the AACGM latitude.

**Figure 12.** (a) MLAT altitude slices of multibeam observations of the density profile from 1025 to 1031 UT. The time labeled on the top of each panel marks the center of the integration time of the panel. (b) Same as Figure 12a but for the interval 1058–1103 UT.

**Figure 12.** (continued)

**Figure 13.** Density profiles sampled within 67° ± 0.25° MLAT, −94.4° ± 2° MLON. (a) Open circles denote the preflow measurements at 1025 UT, while solid circles denote the measurements at 1031 UT, and (b) open circles denote the preflow measurements at 1058 UT, while solid circles denote the measurements at 1102 UT, when the southward moving density patch had reached ~67° MLAT. (c) The variation of the peak intensities of red and blue line auroras within 67° ± 0.25° MLAT, during 1024–1032 UT. The line color in the plot corresponds to the actual emission color. Also shown is the electron temperature from TH-C (black line) and TH-B (gray lin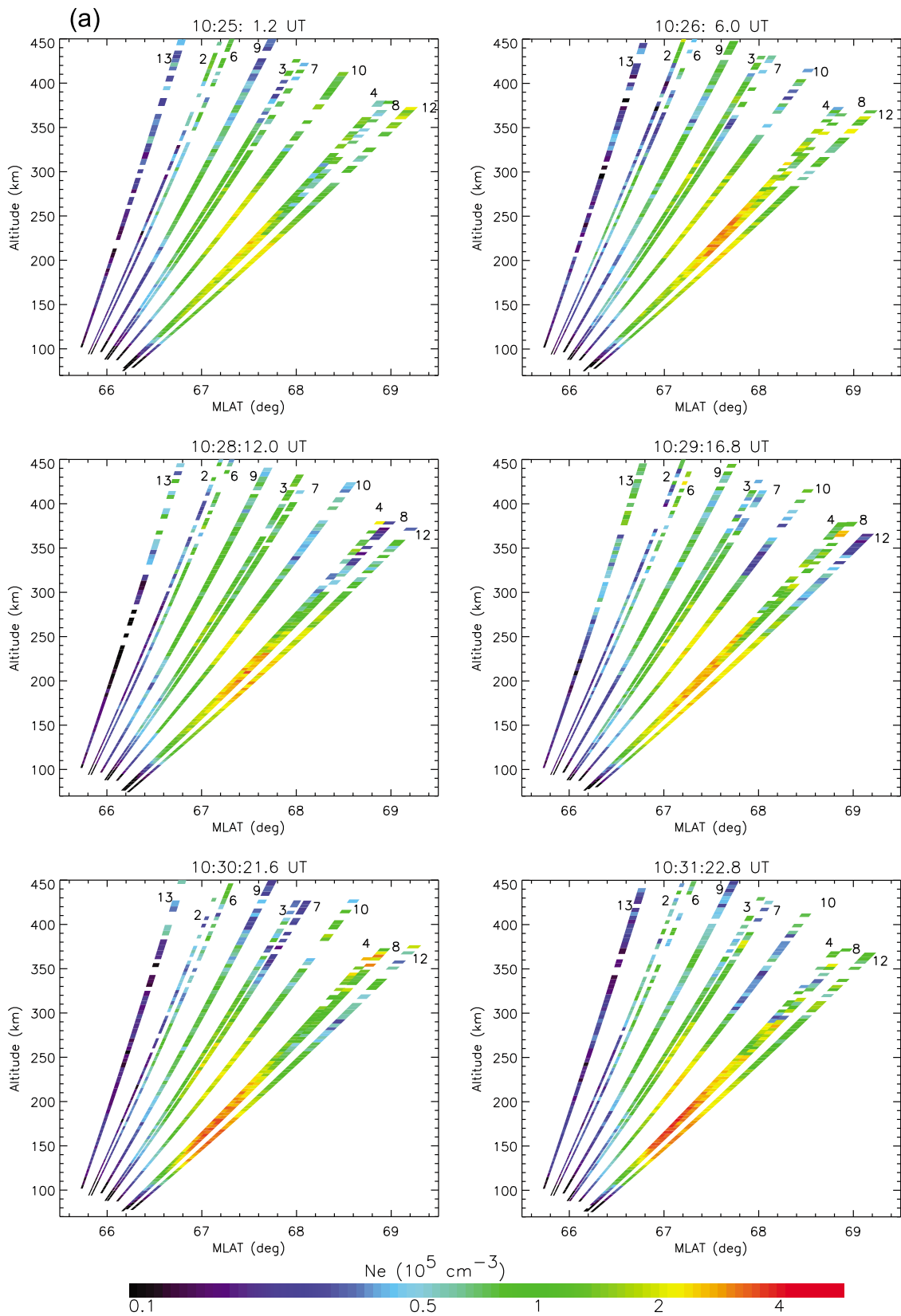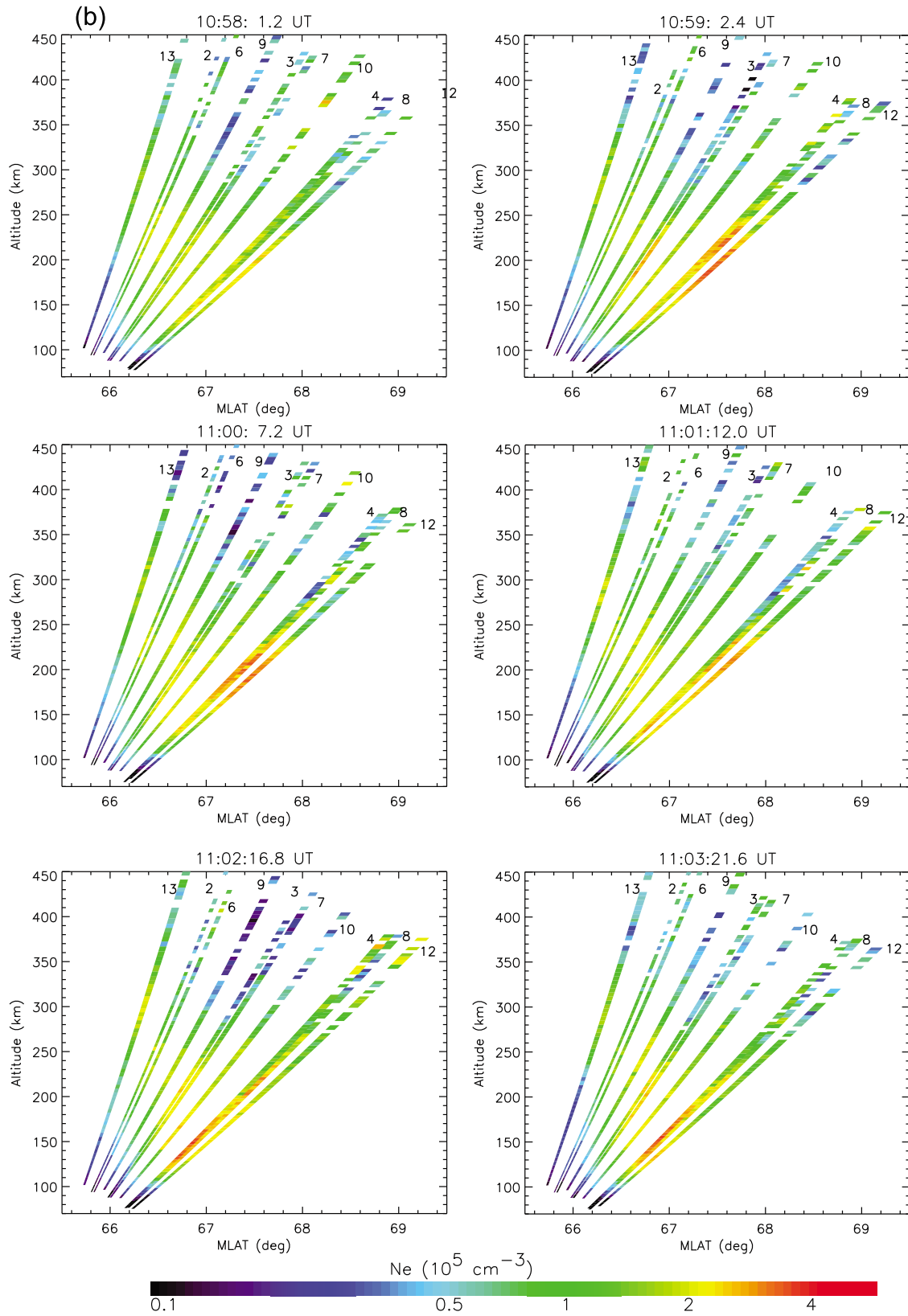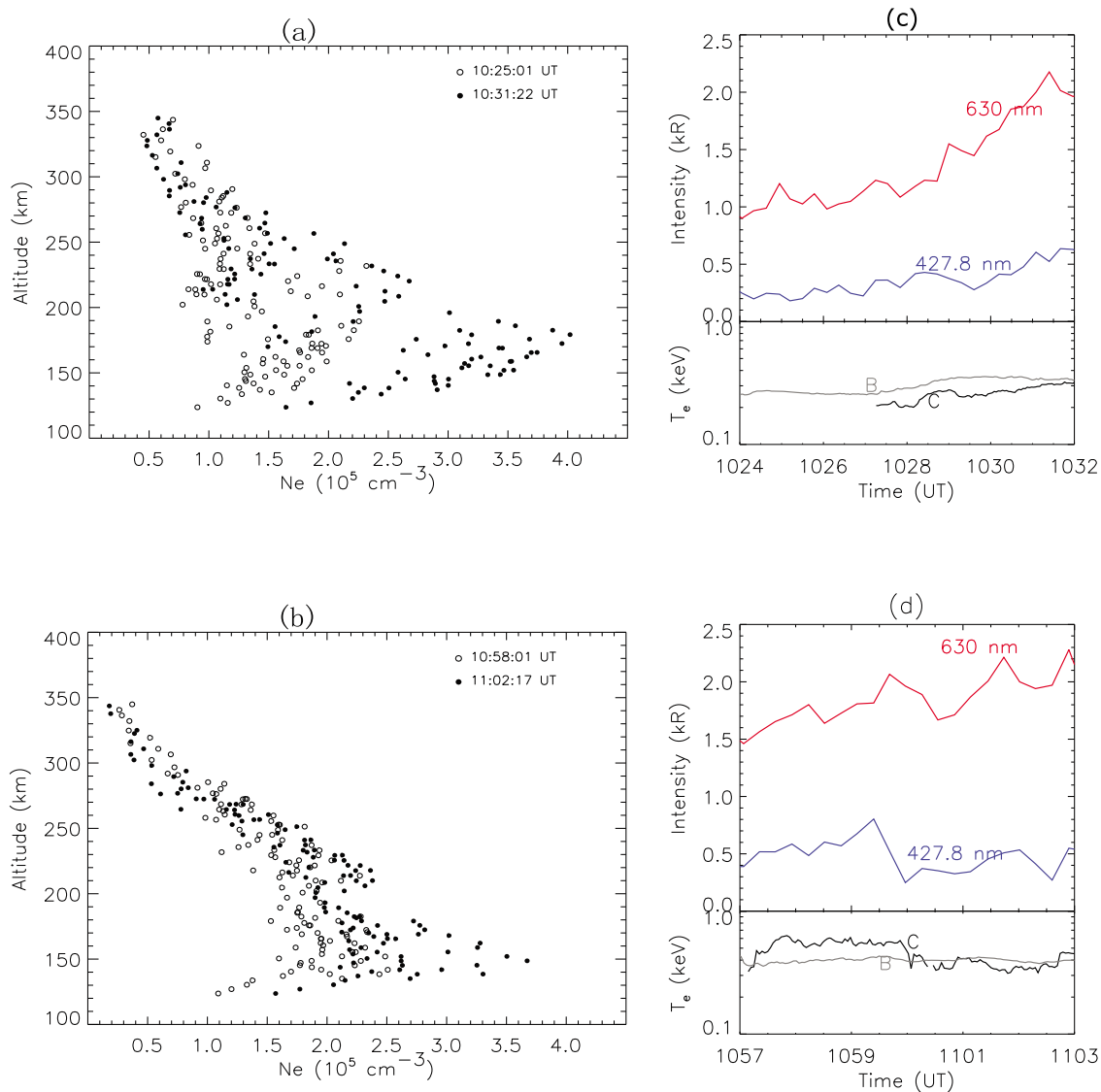e). Gaps in the data indicate the intervals with plasma $\beta$ < 0.5. (d) Same as Figure 13c but for the interval 1057–1103 UT.

general smaller than that in Figure 13 as we may check with Figures 10 and 11.

[39] More inferences on the nature of the precipitation can be drawn from a comparison to the concurrent PFMSP observations. In Figures 13c and 13d we present the peak intensity of red and blue line auroras within 67° ± 0.25 MLAT, the same as we sample the PFISR $N_e$ measurements, over the intervals in Figures 12a and 12b, respectively. Note that by this process we have circumvented the uncertainty of auroral emission height. Enhancements of red line aurora with large red-to-blue ratio are identified during both intervals, dominantly contributing to the equatorward arc

intensifications at ~67° MLAT seen from concurrent white light ASI observations (see Figures 8c and 8i). It is reasonable to conceive that the red line auroral intensification and the $N_e$ enhancement at ~67° MLAT share the same precipitation origin, and both are direct consequence of the earthward flow burst activity. As a useful context for the following discussions we also present in Figures 13c and 13d the electron temperature from TH-B/C observations for both intervals. Data with plasma–$\beta$ < 0.5, i.e., when the probes were far off the CPS, are excluded. The observations show that, while both intervals are characterized with mainly soft CPS electron population, $T_e$ tends to be slightly

higher during the second interval than during the first interval.

## 4. Further Analysis

[40] Section 4 is dedicated to an in-depth theoretical analysis, aided by numerical simulations, on the potential source/mechanism that might account for the observed density patches. We start our analysis from the ionospheric continuity equation:

$$\frac{\partial N_e}{\partial t} + (\mathbf{v} \cdot \nabla)N_e = Q - L, \qquad (2)$$

in which $Q$ and $L$ denote the electron-ion pair production rate and recombination rate, respectively, $\mathbf{v}$ is the ionospheric plasma velocity. Since our observations were confined in the midnight sector, $Q$ was dominated by particle precipitation. The soft electrons of our interest tend to produce ionizations in the $F$ region, which then basically follow the $\mathbf{E} \times \mathbf{B}$ plasma convection. On the other hand, the magnetospheric origin of $Q$, under our notion is also related to the CPS flows. The above scenario provides a qualitative interpretation to the observed southward motion of the ionospheric density patch as shown in Figure 12. We have constructed the altitudinal $N_e$ profiles at ~67° MLAT from multibeam samplings as shown in Figure 13. This latitude is chosen because of a number of reasons. First at this latitude the PFISR beams provide the required altitudinal coverage. Second, in both intervals the southward streaming of the density patch was found "braked" at this latitude, such that the transport term $(\mathbf{v} \cdot \nabla)N_e$ is presumably smaller than the local production rate. Third, that the flow was "braked" also implies that it had entered a transition region from the midtail to the inner plasma sheet, making it more sensible to link the involved precipitation to the in situ THEMIS observations which were also located in such a transition region. The in situ flows were strongly decelerated at the position of TH-B/D/E ($X \sim -11$ $R_E$), we deduce that this distance was roughly the inward extent of the fast earthward flows and presumably mapped to ~66.5° MLAT, according to the radar density observations shown in Figure 12.

[41] In sections 4.1–4.3 we shall first make a semiquantitative estimation of the characteristic energy of the precipitating electrons responsible for the observed density patch, and then evaluate the possible roles of two major mechanisms known as responsible for the precipitation enhancement: the wave-induced pitch angle scattering in the CPS, and the field-aligned acceleration by a parallel potential drop.

### 4.1. Numerical Calculation of the Ionization Profile of Precipitating Electrons

[42] Here we shall numerically calculate a set of ionization profiles of precipitating electrons with different characteristic energies, and then compare the results with the radar and in situ observations shown in Figure 13. The involved procedure in such calculation is rather standard, and can be found in literature such as that by *Rees* [1989] and *Semeter et al.* [2005]. We only summarize below a few key models and assumptions involved in our calculation.

[43] 1. The altitudinal profile of the neutral atmosphere is taken from the MSISE-90 neutral atmospheric model, with parameters such as the AE index and daytime F10.7 flux from actual observations on the event date. The densities of three dominant neutral compositions, $N_2$, O and $O_2$ from the model are shown in Figure 14a.

[44] 2. The differential flux spectrum of precipitating electrons is assumed to have the form

$$j(E) = \frac{\Phi_0}{E_0^2} \cdot E \cdot \exp\left(-\frac{E}{E_0}\right), \qquad (3)$$

in which $E_0$ defines the characteristic energy. In absence any auroral acceleration process, $E_0$ would be essentially equivalent to the CPS $T_e$ for a filled loss cone.

[45] 3. The altitudinal profile of the energy deposition rate of an incident electron is calculated according to the empirical energy range relationship in work by *Rees* [1989].

[46] 4. In evaluating the recombination term in equation (2), for the $F$ region ionosphere of interest we consider only the dissociative reactions involving $O^+$ ions. The reaction coefficients are computed according to the empirical formulas assembled in Table 1 of *Semeter et al.* [2005]. The required parameters, i.e., ionospheric $T_e$ and $T_i$, and the ratio of $O^+$ to the total ion density, are all deduced from the real PFISR measurements. Figures 14b–14d give the ACF-fit $O^+$ ratio, $T_e$ and $T_i$ data, in 3 min integration time, sampled from all beams within 67° ± 0.5° MLAT, −94.4° ± 5° MLON around 11 UT. The gray lines denote their error-weighted polynomial regression, which are then used in our calculations of the recombination coefficients.

[47] 5. For the altitude range of interest 150–190 km, where the strongest density enhancements were found in Figure 13, the recombination time scale calculated from the above procedure ranges between 100 and 300s, which is comparable or smaller than the typical BBF duration [*Angelopoulos et al.*, 1994; *Cao et al.*, 2006]. We assume that the background (preflow) ionosphere is in an equilibrium state, and that the new precipitation source associated with the fast flows has a common duration of 5 min; we then compute the altitudinal profile of the ionization enhancement over this interval as our final simulation output.

[48] Figure 15 gives the resulting ionization profiles for different characteristic energies from 100 to 500 eV. We have normalized the differential flux spectrum in equation (3) with a total precipitation flux $\Phi_0 = 10^8$ cm$^{-2}$s$^{-1}$ in our calculations. Admittedly the above approach is contingent upon a number of external models and empirical formulas. Therefore, our calculation may be better described as semiquantitative only, but nevertheless provide helpful references for us to infer the energy spectra of the observed precipitation. Seen from Figures 13a and 13b the peak heights are roughly located around ~180 km and ~150 km, respectively. Comparing to Figure 13 we infer that the characteristic energy of the precipitation would be at (Figure 13a) 200–300 eV and (Figure 13b) 400–500 eV, respectively. Interestingly, notwithstanding our model uncertainties and the displacement of the probes to the radar meridian, the above estimations are rather comparable to the in situ observed CPS electron temperature on TH-C and TH-B during the same periods. This match points to a
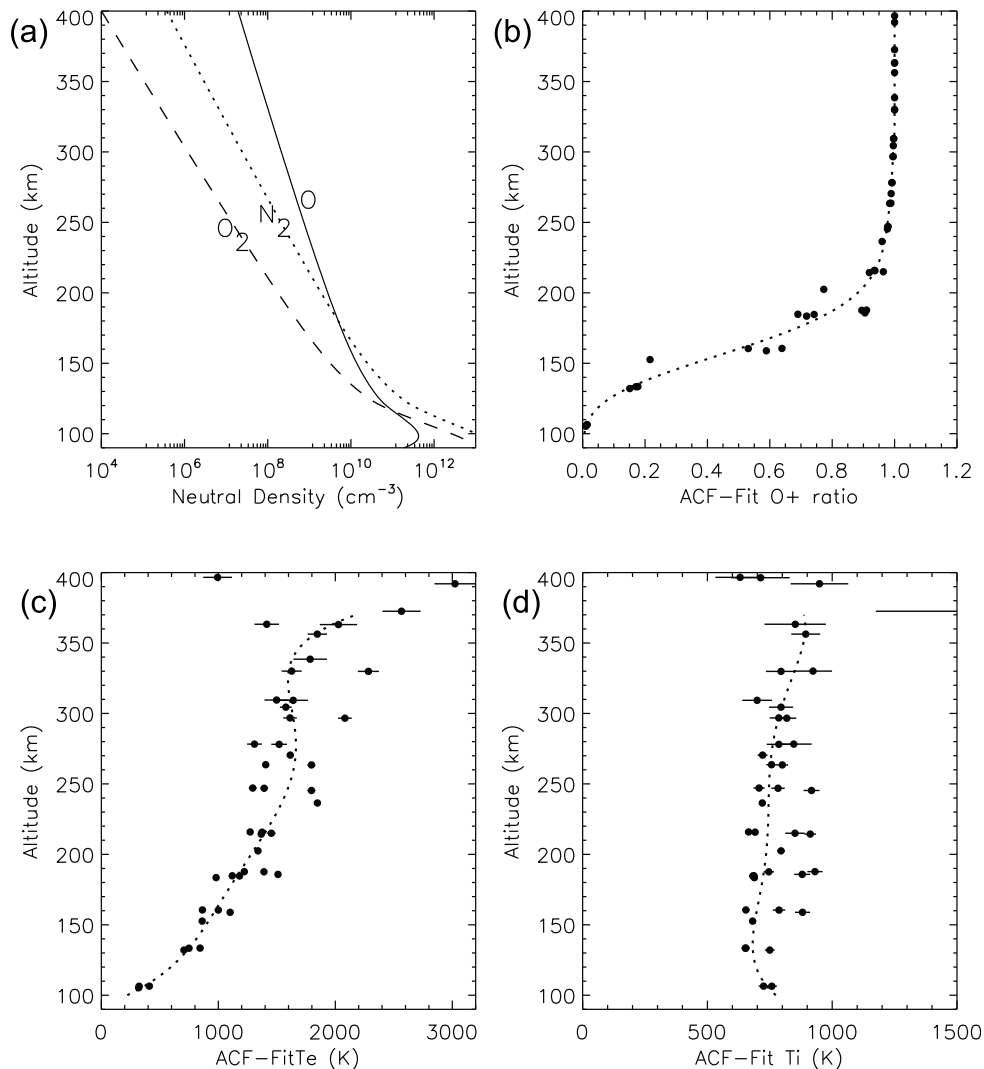
**Figure 14.** (a) Number densities of $N_2$, $O_2$, and O obtained from the MSISE-90 model. (b–d) ACF-fit $O^+$ ratio, $T_e$, and $T_i$, in 3 min integration time, sampled from all beams within $67° \pm 0.5°$ MLAT, $-94.4° \pm 5°$ MLON around 1100 UT. The horizontal dashes in the $T_e$ and $T_i$ plots denote their standard errors in the ACF-fit data set. The gray dotted lines denote an error-weighted fifth-order polynomial regression of $O^+$ ratio, $T_e$, and $T_i$, which will be used in our calculation of the reaction coefficient.

direct linkage between the observed precipitation and the magnetospheric electrons.

### 4.2. Possible Role of ELF Waves and Pitch Angle Scattering of CPS Electrons

[49] Based upon the results in section 4.1, we shall evaluate here whether the wave-particle interaction can be a viable mechanism in pitch angle scattering the soft electron population in the CPS, and whether the resulting fully filled loss cone adequately account for the observed ionization enhancement.

[50] We have shown in Figure 4 that accompanying the fast flows there were broadband ELF wave enhancements extending to the vicinity of the electron gyrofrequency $f_{ce}$. The existence of flow-driven plasma turbulence has been recognized for a long time [e.g., *Vörös et al.*, 2006]. Such plasma turbulence can cause the particle diffusion in

velocity space via wave-particle interactions [*Kennel and Engelmann*, 1966]. In particular, the electron cyclotron resonance is widely understood as the dominant wave-particle interaction process leading to the pitch angle diffusion of CPS electrons. Provided that there is a temperature anisotropy and/or a loss cone property embedded in the electron pitch angle distribution, certain bands of the wave spectrum may further grow out of the background turbulence (see Figure 4c), two well-known examples of this process being the whistler mode chorus and the electron cyclotron harmonic (ECH) wave [e.g., *Kennel and Petschek*, 1966; *Kennel et al.*, 1970]. We admit that lower-frequency turbulence convecting with fast flows may be Doppler shifted to higher frequencies and appear as extending spectrum on satellite measurements, yet they may not necessarily resonate with electrons. A more dedicated and extensive survey on the conjunction between the fast flows
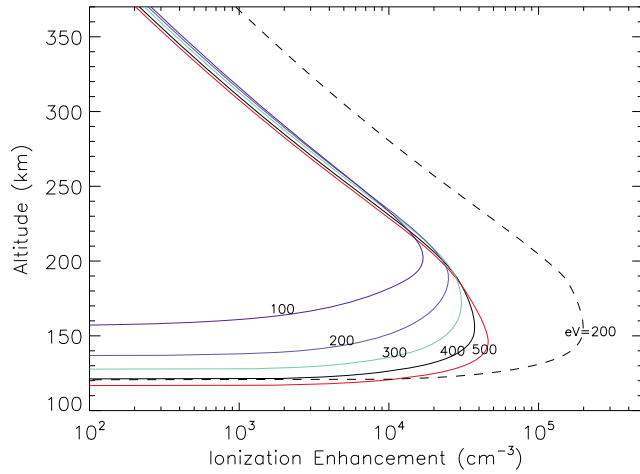
**Figure 15.** Ionization enhancement profiles calculated from the model and equations depicted in the text. The precipitation is normalized to total flux of $10^8$ cm$^{-2}$ s$^{-1}$, but with different characteristic energies $E_0$ from 100 to 500 eV, as labeled on each line. The dashed line corresponds to the case of $n = 1$ cm$^{-3}$, $T_e = 400$ eV but with a parallel potential drop of 200 eV (see equation (6)).

and ELF waves in the midtail CPS is undergoing in a separate study (J. Liang, manuscript in preparation, 2011), from which we statistically confirm that the ELF waves over broad frequency range consistently intensify with flow enhancement, and tentatively conclude that a majority of the observed waves in the whistler mode frequency range do not owe their existence to the Doppler shift of lower-frequency turbulence. Under such notion, in the present paper we shall briefly discuss the implications of the midtail CPS conditions to the whistler cyclotron resonance and the resulting pitch angle scattering process at the equatorial plasma sheet. The minimum electron energy required for such resonance is given by [*Kennel and Petschek*, 1966]

$$E_{res} = \frac{B_{eq}^2}{2\mu_0 n} \cdot \frac{(1 - f')^2 \cdot (\cos\theta - f')}{f' \cos^2\theta}, \qquad (4)$$

in which $f' = f/f_{ce}$, namely the ratio of the wave frequency to the electron gyrofrequency; $B_{eq}$ is the equatorial magnetic field, and $n$ is the equatorial plasma density; $\theta$ is the wave normal angle. Using the example shown in Figure 4 we assume $f' = 0.7$, and $B_{eq} = 5$–$10$ nT and $n = 0.5$–$1$ cm$^{-3}$, representative of the conditions from midtail to near-tail CPS of flow passage. We then deduce from (4) that the minimum resonant energy would be on the order of ~100 eV or less. Therefore, a majority of the CPS electrons may participate in the cyclotron resonance and undergo pitch angle scattering. On the other hand, existing ECH theories and simulations also revealed that the ECH wave can effectively interacts with electrons of a few hundred eV [*Tripathi and Singhal*, 2009; *Ni et al.*, 2011], and the resonant energy would also reduce with decreasing $B_{eq}$. In short, we propose that flow-driven ELF waves may interact with the ambient CPS electrons via cyclotron resonance, and in turn cause their diffusion into the loss cone. The process is conceptually similar to the generation of diffuse auroras in

the inner magnetosphere, but the resonance would be biased to much lower energy range in the outer magnetosphere due to small $B_{eq}$, particularly under thinned CPS conditions.

[51] We then confront with the question that whether a filled loss cone alone can be responsible for the observed $N_e$ enhancement. The peak ionization increment is about 1.5–2 $\times 10^5$ cm$^{-3}$ for both intervals in Figure 13. To produce such density increment from electron precipitation with $E_0 = 400$eV, we infer from Figure 15 that a precipitation flux of $4.0$–$5.3 \times 10^8$ cm$^{-2}$s$^{-1}$ is required. Assuming a fully filled loss cone with isotropic Maxwellian distribution, the precipitation flux mapped to the ionosphere, in absence of any acceleration process, is given by

$$\Phi_{loss} = n \cdot \sqrt{\frac{T_e}{2\pi m_e}}, \qquad (5)$$

where $n$ is the plasma number density; $T_e$ is electron temperature which in this context is equivalent to $E_0$; $m_e$ is the electron mass. Assuming $n = 1$cm$^{-3}$ and $T_e = 400$eV, the loss cone flux would be ~3.3 $\times 10^8$ cm$^{-2}$s$^{-1}$. As noted above the density patch under investigation in Figures 12 and 13 represented nearly the high end of the observed $N_e$ enhancement, but on the other hand the loss cone could not be entirely empty even in absence of the flow activity, since there were nonvanishing red line emissions then. Taking into account the above considerations, as well as the uncertainties involved in the numerical model and in the observations, we suggest that a fully filled magnetospheric loss cone tends to be slightly inadequate to account for the upper end of the observed ionization enhancement.

### 4.3. Possible Role of the Parallel Potential Drop

[52] Since the magnetospheric loss cone flux is limited it has long been realized that a field-aligned electron acceleration is often required to accommodate the FAC produced in the magnetosphere [e.g., *Knight*, 1973]. The possible role of such parallel acceleration is to be evaluated here. As above mentioned the observed density patches at ~67° MLAT were accompanied by equatorward arc intensifications at the same latitude. We speculated that when the fast flows were undergoing a transition from midtail to near tail the flow deceleration/diversion, evidenced by the dramatic decrease of flow magnitude between TH-C and TH-B, would give rise to FACs that might summon the presence of a parallel potential drop. Such FAC though, could not be intense since the ground magnetic disturbances were found as rather moderate. Also, concurrent PFMSP observations revealed that those equatorward arc intensifications were mainly composed of red line emission, implying a soft electron origin. There was no LEO satellite passage over the FOV of interest during the event interval; we are thus not in a position to fully evaluate the role of the auroral acceleration. However, a semiquantitative estimation of the effect of such parallel potential can be made as follows. We consider the following shifted Maxwellian distribution:

$$f(E) = n \left(\frac{m_e}{2\pi T_e}\right)^{3/2} \cdot \exp\left(-\frac{E - eV}{T_e}\right) \quad E > eV, \qquad (6)$$

where $V$ denotes the parallel potential drop. We calculate the impact ionization by a precipitation flux spectrum specified

by (6) according to the above depicted procedures. In Figure 15 the dashed line show the result with $eV = T_e/2 = 200$ eV, namely the parallel potential drop is half the electron temperature. Note that different from other lines in Figure 15, which are normalized to a flux of $10^8$ cm$^{-2}$s$^{-1}$, the dashed line is directly calculated from (5) with $n = 1$ cm$^{-3}$ and $T_e = 400$ eV, and thus features a magnetospheric loss cone flux of $\sim 3.3 \times 10^8$ cm$^{-2}$s$^{-1}$ as above mentioned. One can see that a moderate parallel acceleration may substantially enhance the ionization rate, yet not alter the peak altitude of the ionization. With the parameters chosen the ionization enhancement peaks at $\sim 150$ km height, similar to the case without parallel acceleration (solid black line), with a maximum of about $2 \times 10^5$ cm$^{-3}$, in good agreement with the magnitude of observed $N_e$ enhancement. Via test simulations we further find that, when the parallel potential is higher than $T_e$ the resulting ionizations tend to shift to lower altitudes with unrealistically high magnitude as compared to the observations, which is understandable in that a strong parallel potential drop would harden the overall precipitation spectrum and dramatically increase the precipitation flux. From the above calculations we deduce that the observed flow-driven density enhancements were likely associated with a moderate auroral acceleration, but the involved parallel potential was comparable to or smaller than the CPS $T_e$. This constraint is not trivial, since the relative magnitude of the parallel potential drop as compared to $T_e$ is one of the key factors differentiating the underlying mechanisms of such potential; it has led to, for example, the distinction between the "strong double layers" [e.g., *Mozer and Kletzing*, 1998] and "weak double layers" [e.g., *Mälkki et al.*, 1993]. Also, parallel electric fields supported by magnetic mirror forces, one of the classical self-consistent theories on maintaining a quasi-static parallel potential drop [e.g., *Ponyavin et al.*, 1977], require trapped particle populations with energies comparable to or larger than the field-aligned potential difference being maintained.

## 5. Discussion

[53] Fast plasma flows in the magnetosphere are expected to produce dynamic auroral and ionospheric features. Until recently, however, the connection between the two has not been systematically investigated due to a lack of overlapping coverage and limitations in instrumentation. The deployment of THEMIS and PFISR, coupled with existing ground-based auroral imagers, allowed us to undertake one of the first quantitative comparisons in this regard. We found that there are two types of auroral emissions: The first is associated with PBIs (>68° MLAT) is dominated by energetic electron (>1 keV) precipitation. The second is associated with the equatorward moving features emanating from the first type, but is dominated by soft electron (<1 keV) precipitation. The first class is likely related to the physical process (e.g., magnetic reconnection) that gives rise to the fast flow, whereas the second may be the result of flow bursts moving through ambient plasma that contains predominantly soft electrons. The fast flows cause the new plasma intrusion into the near-Earth CPS, which is deemed as one possible triggering mechanism of the substorm onset [*Nishimura et al.*, 2010; *Lyons et al.*, 2010]. In a nonsubstorm event as

in this paper, the in situ observations revealed that, despite the strong flow activities the electrons in the near-Earth CPS remained essentially soft in absence of high-energy population. This observation can be understood as follows. The fast flows are well known to have limited cross-tail dimension [e.g., *Nakamura et al.*, 2004]. While it is likely that the process producing the flow bursts also produce the energetic electrons, those "hot" electrons undergo much faster drift loss from the flow channel. Assuming a cross tail width of $\sim 2$ R$_E$ and a curvature/gradient drift speed of $\sim 50$ km/s typical of high-energy electrons, the lifetime of those electrons in the flow channel is no more than $\sim 4$ min. The finite width of the fast flow channel also limit the maximum energy an ambient electron can obtain from the adiabatic acceleration by the flows. Therefore, it is understandable that there would be a transition between the dominances by the energetic and soft electron populations, contingent upon the width of the flow channel. The higher-energy electrons are more radially confined to its origin, e.g., the reconnection site, while the lower-energy electrons tend to more or less follow the trajectory of the flows and penetrate closer to the Earth. In this regard, the soft electron precipitation may give direct trace of, and have inherent relationship to, the fast flows. This flow-related soft electron precipitation, also suggested in a few recent studies relating the magnetospheric flows to the red line auroras [*Kepko et al.*, 2009; *Lui et al.*, 2010; *Spanswick et al.*, 2009], is of the core research interest in this paper and is investigated in unprecedented detail by utilizing the PFISR technique.

[54] Based upon the observations presented in section 3, and the analyses on the characteristic energy and the ionization magnitude of precipitating electrons presented in section 4, we suggest that the observed flow-related precipitation is contributed by an enhanced pitch angle diffusion of the CPS electrons into loss cone via wave-particle interactions, with the aid of a moderate parallel potential drop comparable to or smaller than the CPS $T_e$. The precipitation prescribed by the above mechanisms has limitations in terms of both the characteristic energy (limited by the CPS $T_e$ and the electron resonant energy), and the precipitation flux (not exceeding by far a filled magnetospheric loss cone). During later substorm growth phase [e.g., *Kepko et al.*, 2009] and spontaneous fast flow intervals (as in this study) the midtail CPS is typically much stretched with low $T_e$, leading only to soft electron precipitation with relatively weak fluxes.

[55] Some of our observed features, such as the latitudinally extended red line auroras observed by PFMSP, and the associated equatorward moving density patches observed by PFISR, show certain resemblance to the classical aurora "streamer" activity that has been widely considered as the ionospheric manifestations of the fast earthward flows in the midtail plasma sheet. However, we emphasize one key difference between our reported feature and the classical auroral streamer: the streamers in existing literature are often found to feature a hard electron precipitation component [e.g., *Zesta et al.*, 2000; *Sergeev et al.*, 2004], while in our event the structure is made primarily of soft electron precipitation. In this regard, the streamer was often interpreted as driven by the strong FAC (which naturally implies strong parallel acceleration) due to the flow/magnetic shear

along the flankside of a flow channel [e.g., *Nakamura et al.*, 2001; *Sergeev et al.*, 2004], while as discussed above the interpretation to our observed feature is essentially a scattering process by flow-driven ELF waves. Our propose mechanism might explain why the streamers are sometime not seen as accompanying the CPS fast flows, from auroral imagers that are more sensitive to energetic electron precipitation. Obviously, based upon an event study we are not in a position to compare our proposed mechanism to other candidate mechanisms in terms of their prevalence. It would be an interesting research direction in the future to investigate under what magnetospheric condition one mechanism might prevail over the others, and lead to primarily hard or soft precipitation associated with fast flows.

[56] One other important precipitation type, so-called the "Alfvenic" aurora, invokes the time-dependent electron acceleration by inertial/kinetic Alfven waves [*Chaston et al.*, 2002; *Lysak and Song*, 2000]. This type of precipitation features broad energy distribution of electrons, extending from tens of eV up to keV range, and hence results in a tall column of $N_e$ enhancement over broad altitude range [e.g., *Semeter et al.*, 2005]. The observations shown in Figures 13a and 13b indicate that there was no substantial density increment at >200 km altitude, which does not support the existence of such Alfvenic auroras. However, we admit that the data quality of the PFISR $N_e$ observations is not good enough to allow for a reliable inversion of the complete energy spectra of the precipitating electrons, nor do the measurements have enough horizontal resolution to resolve the narrow Alfvenic structures (~1 km). We thus may not entirely exclude the possibility of Alfvenic auroral precipitation from available observations. It has long been proposed that when fast flows travel earthward it may perturb the field line and launch Alfven waves on its propagation front [e.g., *Kepko et al.*, 2004; *Liu et al.*, 2008]. *Angelopoulos et al.* [2002] reported the observations of Alfvenic Poynting fluxes associated with the BBFs. The potential role of the flow-driven Alfvenic acceleration remains an issue of future study, presumably with the aid of LEO satellite or rocket observations. There are some other possible ionization sources, e.g., the ionization due to the proton auroral precipitation [*Galand et al.*, 1999; *Zou et al.*, 2009], and the ionization due to the secondary electrons excited when the primary electrons/protons bombards the neutral atmosphere [e.g., *Rees*, 1989]. In particular, the proton auroras and its resulting secondary electrons were also found as capable of producing red line emissions [*Lummerzheim et al.*, 2001], but only under the circumstance of exceedingly large proton precipitation fluxes with high mean energy (~10 keV [see *Lummerzheim et al.*, 2001]). Had it been the case for our event such intense proton precipitation would have induced strong ionization in the E region [e.g., *Galand et al.*, 1999], which was not evidenced from radar observations.

[57] We now turn our attention to the consequences of fast flows inside the inner plasma sheet. During the interval 1025–1100 UT there was a southward expansion of the equatorward aurora border, which is clearly shown from the red line observations in Figure 7. While the in situ fast flows were intermittent throughout the event interval, the motion of the equatorward auroral border was much slower and gradual (~1° in about 30 min), and stalled at ~66° after ~1100 UT. The observations point to the scenario that when intermittent yet consecutive fast earthward flows penetrate into the inner plasma sheet, they are decelerated and joint to cause a gradual reconfiguration of the inner magnetosphere, until a new balance is reached. Gradual southward motion and subsequent saturation of the equatorward border of the auroral bulge associated with earthward propagating dipolarization front during substorm expansion are also reported by *Sergeev et al.* [2010], though in their events the related precipitation was composed of ~10 keV energetic electrons due to strong substorm injection, while in our nonsubstorm event much softer electron precipitation dominated in the inner plasma sheet. The southward expansion of auroras also left distinct imprints on PFISR observations. As mentioned in section 3.4, for those higher elevation angle beams (e.g., beams 2, 6, 9, and 13) that measured latitudes <67° MLAT close to the equatorward auroral border, the density patches obviously lagged in appearance time, as compared to those on low elevation angles beams (e.g., beams 4, 8, and 12) that measured more poleward latitudes. One salient feature which was clearly shown by radar observations but could not be resolved with optical measurements is that, aside from the time lag the density enhancement was found to be confined to higher altitudes with decreasing latitudes. Such trend can be inferred from the cross-beam variations shown in Figures 10 and 11, or identified from the MLAT altitude $N_e$ profiles in Figure 12 between 66 and 67° MLAT, where the altitudinal coverage of the measurement is sufficient. More specifically, since beam 13 is near vertical (elevation ~83°) its observation can be used as a proxy of the local vertical $N_e$ profile. As one can see from Figure 10 (bottom) the density patch emerging at ~11 UT was located at about 230–350 km height, distinctly higher than those detected by poleward beams. From the continuity equation (2), the appearance of higher-altitude density patch may result from a precipitation source of lower characteristic energy, and/or a substantial upward motion of the ionospheric plasma (e.g., carried by strong upward neutral wind). While we may not exclude the latter possibility, we argue that the former is more reasonable and can be explained by an "electron Alfven layer" effect originated from the differential adiabatic drift of soft electrons as follows.

[58] For mathematical straightforwardness we shall limit the following discussion to trapped electrons (90° pitch angle) and electrostatic convection. The trajectory of a trapped electron at the equatorial CPS follows the contour of constant $\mu B - e\Phi$, in which $\mu$ is the first adiabatic invariant, $B$ is the equatorial magnetic field, and $\Phi$ is the electric potential. Inferred from the PFISR VLOS pattern (Figure 9) the fast flows are in general east-earthward. For soft electrons the electric drift dominates in the midtail where $\mu B$ is negligibly small, such that they all follow the convective flow streamlines (i.e., equipotential contours) regardless of $\mu$. However, when they approach the inner magnetosphere they undergo increasing $\mu$-dependent gradient drift. Higher-$\mu$ electrons will be more subject to eastward gradient drift, while lower-$\mu$ electrons will be less subject to the gradient drift and thus penetrate closer to the Earth. Assuming two electrons originate from the same potential contour $\Phi_0$ in the midtail where $B$ is small, but with different $\mu$ ($\mu_2 > \mu_1$). When these two electrons drift into the inner plasma sheet and cross the projection line of the radar

```
┌──────────────────────────┐                              ┌──────────────────────┐
│ Magnetospheric           │─────────────────────────────▶│ Auroral PBI          │
│ Fast Flow                │                          │   │ Sect. 3.3, Fig. 7& 8 │
│ Sect. 3.2, Fig. 3        │                          │   └──────────────────────┘
└──────────────────────────┘                          │
         │                                             │   ┌ ─ ─ ─ ─ ─ ─ ─ ─ ─ ─ ─ ─ ─ ─ ─ ─ ─ ─ ┐
         │          ┌ ─ ─ ─ ─ ─ ─ ─ ─ ─ ─ ┐           │
         ▼          │ Moderate FACs from   │           └──▶│ Latitudinally-extended red-         │
┌──────────────────┐ │ flow deceleration ? │               │ line aurora and southward-          │
│ ELF wave         │ │ Sect. 4.3           │               │ moving density patch                │
│ intensification  │ └ ─ ─ ─ ─ ─ ─ ─ ─ ─ ─ ┘               │ Sect. 3.3 & 3.4, Fig. 7&10&12      │
│ Sect. 3.2, Fig. 4│                                        │
└──────────────────┘                                        │ ┌──────────────────────┐
         │                                                  │ │ Equatorward arc intensifi-│
         ▼                                                  │ │ cation and density patch at│
  ┌ ─ ─ ─ ─ ─ ─ ─ ─ ─ ─ ┐                                   │ │ ~67 MLAT             │
  │ Pitch-angle diffusion│──────────────────────────────────▶│ Sect. 3.3 & 3.4, Fig. 8&12&13│
  │ of soft electrons    │                                   │
  │ Sect. 4.1 & 4.2      │                                   │ Soft Electron Precipitation
  └ ─ ─ ─ ─ ─ ─ ─ ─ ─ ─ ┘                                   │
         ▲                                                   │ ┌──────────────────────┐
┌──────────────────┐                                        │ │ Increase of precipitation│
│ Mainly soft CPS  │                                        │ │ altitude toward equatorward│
│ electrons        │                                        │ │ auroral border        │
│ Sect. 3.2, Fig. 3&5│                                      │ │ Sect. 3.4, Fig. 10&11 │
└──────────────────┘                                        │ └──────────────────────┘
         ▲                                                   └ ─ ─ ─ ─ ─ ─ ─ ─ ─ ─ ─ ─ ─ ─ ─ ─ ─ ─ ┘
  ┌ ─ ─ ─ ─ ─ ─ ─ ─ ─ ─ ┐
  │ Electron Alfven layer│─────────────────────────────────▶
  │ effect in inner CPS  │
  │ Sect. 5              │
  └ ─ ─ ─ ─ ─ ─ ─ ─ ─ ─ ┘
         ▲
┌──────────────────┐
│ Convection pattern│
│ in inner CPS     │
│ Sect. 3.4, Fig. 9│
└──────────────────┘
```
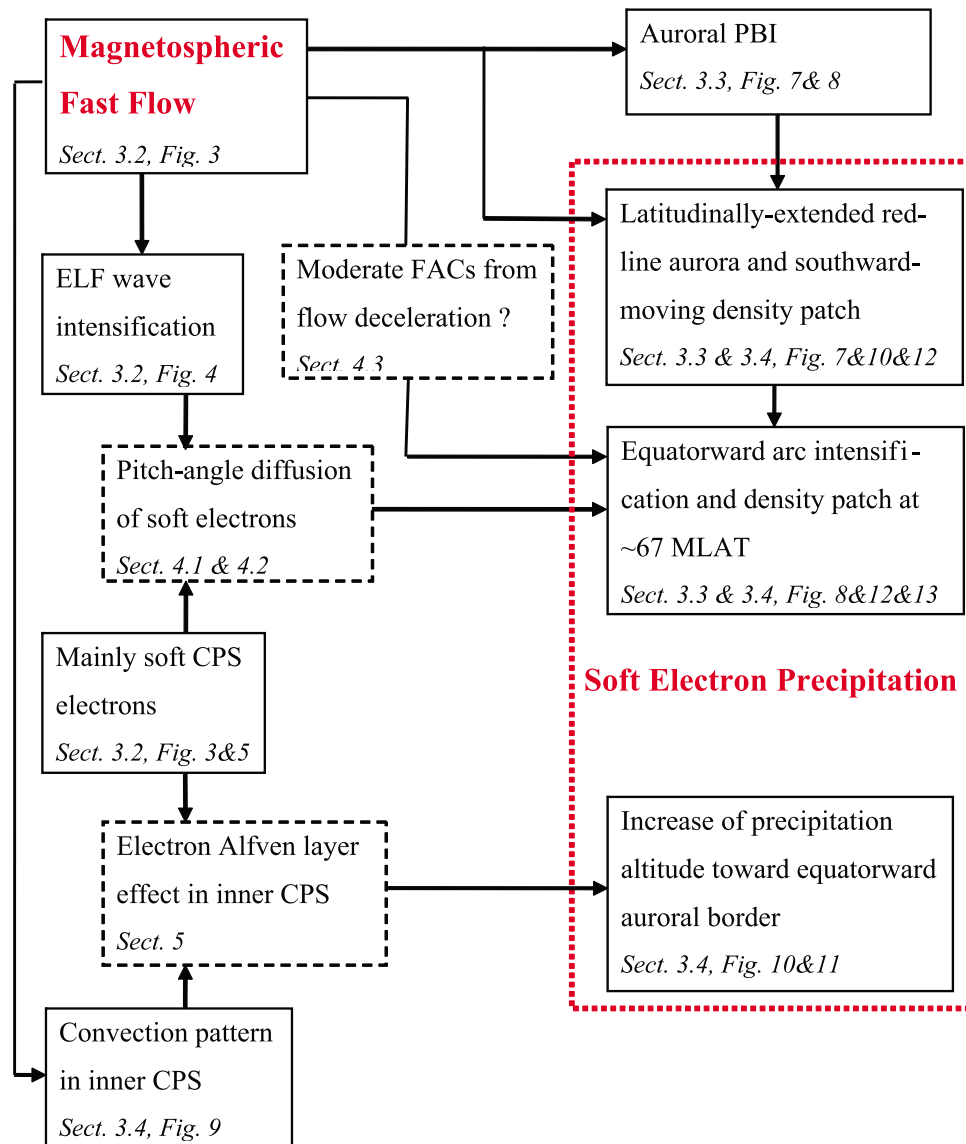
**Figure 16.** A schematic chart threading all key observations and our proposed scenarios in this study. For each observation we also provide its description section and relevant figure(s) in the paper. An arrow indicates that a cause-effect relationship and/or consequential phenomenon are deemed in our scenario. Dashed-line boxes indicate that the interpretations are aided with numerical and theoretical analyses. A dotted-line box encompasses our major interest of this study, i.e., the soft electron precipitation.

meridian in the equatorial CPS, the two electrons are separated by both radial distances (labeled as $r_1$ and $r_2$, respectively) and potential contours, prescribed by the following relationship:

$$-e\Phi_0 = \mu_1 B(r_1) - e\Phi(r_1) = \mu_2 B(r_2) - e\Phi(r_2). \qquad (7)$$

[59] The above analyses on the electron drift trajectory imply that $r_2 > r_1$ and $\Phi(r_2) > \Phi(r_1)$, the latter being a corollary of the eastward flows in the inner plasma sheet. We thus have $\mu_2 B(r_2) > \mu_1 B(r_1)$; that is, the outer electron has higher thermal energy than the inner one. Furthermore, considering the flow-carried electron fluxes are contained within a finite width fast flow channel in the midtail, whose duskside boundary is delimited by a potential $\Phi_B$, the upper energy limit of the electrons reaching the point $r_1$ is $e[\Phi(r_1) - \Phi_B]$, while is $e[\Phi(r_2) - \Phi_B]$ at point $r_2$; again the latter is higher. The above process would lead to a decrease of the average electron energy toward the inner edge of the electron plasma sheet, which is morphologically necessary to allow for a smooth transition from CPS electrons to cold plasmaspheric electrons, similar to the well-known "ion Alfven layer" effect in the evening sector.

[60] Another natural deduction from the above electron drift scenario is that the combination of the earthward convection and the curvature/gradient drift would lead to a "tilted" inner edge of the electron plasma sheet: the electrons may penetrate closer to the Earth when they drift more toward the east. In Figure 11 we have noticed that

though beam 1 and 5 measure roughly the same latitudes (~66° MLAT), the density patch is well discernible on eastward beam 5 but not so on westward beam 1. This observation implies that the equatorward auroral border, on its southward expansion in response to the flows, reached lower latitudes on the eastside of the radar meridian than on the westside, which is fully consistent with the theoretical expectation.

[61] The above analyses explain the trapped particle source in the inner plasma sheet. To account for the electron precipitation an upward FAC is also needed to be present. Such upward FAC would presumably be part of the region 2 current system and be associated with a duskward pressure gradient, which is indeed found to persist in the near-midnight inner plasma sheet during nonsubstorm intervals based upon recent THEMIS survey [*Xing et al.*, 2009].

## 6. Summary and Conclusion

[62] Based upon a comprehensive data set of in situ and ground-based observations we have detailed the dynamic variations of optical auroras and ionosphere electron densities during an interval of a series of fast flows in the tail. A schematic chart threading all key observations and our proposed scenarios is provided in Figure 16. One particular and favorable feature of this event lies in that it was neither preceded nor ensued by a substorm activity. Therefore, the ionospheric signature under investigation would be more liable to be directly linked to the fast flow itself, without being complicated by the formidable complexity of substorm processes. A main theme of this study is to combine the optical auroral and PFISR measurements to infer the 4-D (latitude, longitude, altitude, and time) properties of the precipitation, and to deduce the incident electron characteristics and their potential linkage to the tail flow dynamics inferred from THEMIS in situ observations. Major results of this study include the following.

[63] 1. During the event interval TH-C in the midtail detected a series of fast earthward flow bursts, which were accompanied by prominent intensifications of optical auroras and ionospheric $Ne$. We found that the flow-related auroral activities consisted of intermittent PBIs, which was attributed to energetic electron (>1 keV) precipitation, and more latitudinally extended red line (630nm) intensifications Meanwhile, the PFISR observations detected the $N_e$ enhancements dominantly in the $F$ region ionosphere during the fast flow intervals. The general pattern and morphological evolution of the PFISR density profile are consistent with those of the 630 nm auroras, confirming that they were produced by the same source, i.e., the soft electron (<1 keV) precipitation.

[64] 2. We demonstrated the southward motion of ionospheric density patches in conjunction with the earthward flow bursts and auroral activations. By virtue of the multibeam observations of PFISR we are able to construct the altitudinal profiles of $N_e$. Via semiquantitative model calculations we estimate that the characteristic energies of the incident electrons producing the density patches were at most a few hundred eV, which is comparable to the observed CPS electron temperature.

[65] 3. Based upon the observations and theoretical considerations we suggest the following scenarios associating the fast flow with the soft electron precipitation. The fast flows give rise to enhanced ELF wave activities, which cause strong pitch angle diffusion of the soft electrons in CPS via wave-particle interaction such as the electron cyclotron resonance. The precipitation may be further aided with a moderate field-aligned potential drop comparable to or smaller than the CPS electron temperature, which is likely related to the FACs generated by the flow deceleration/diversion in the near-Earth CPS.

[66] 4. We inferred from PFISR observations that toward the equatorward auroral border there was an ascending trend of the altitude range of the density patches with decreasing latitudes, and that the density patch penetrated to lower latitudes on the eastside of the radar meridian than on the westside. The above features were found as consistent with the theoretical expectations from the adiabatic motion of soft electrons, consisting of their convective and curvature/gradient drifts inside the inner plasma sheet.

## References

Angelopoulos, V. (2008), The THEMIS mission, *Space Sci. Rev.*, *141*, 5–34, doi:10.1007/s11214-008-9336-1.
Angelopoulos, V., C. F. Kennel, F. V. Coroniti, R. Pellat, M. G. Kivelson, R. J. Walker, C. T. Russell, W. Baumjohann, W. C. Feldman, and J. T. Gosling (1994), Statistical characteristics of bursty bulk flow events, *J. Geophys. Res.*, *99*, 21,257–21,280, doi:10.1029/94JA01263.
Angelopoulos, V., et al. (2002), Plasma sheet electromagnetic power generation and its dissipation along auroral field lines, *J. Geophys. Res.*, *107*(A8), 1181, doi:10.1029/2001JA900136.
Auster, H. U., et al. (2008), The THEMIS fluxgate magnetometer, *Space Sci. Rev.*, *141*, 235–264, doi:10.1007/s11214-008-9365-9.
Bonnell, J. W., et al. (2008), The electric field instrument (EFI) for THEMIS, *Space Sci. Rev.*, *141*, 303–341, doi:10.1007/s11214-008-9469-2.
Brekke, A., C. Hall, and T. Hansen (1989), Auroral ionospheric conductances during disturbed conditions, *Ann. Geophys.*, *7*, 269–280.
Cao, J. B., et al. (2006), Joint observations by Cluster satellites of bursty bulk flows in the magnetotail, *J. Geophys. Res.*, *111*, A04206, doi:10.1029/2005JA011322.
Chaston, C. C., J. W. Bonnell, L. M. Peticolas, C. W. Carlson, J. P. McFadden, and R. E. Ergun (2002), Driven Alfven waves and electron acceleration: A FAST case study, *Geophys. Res. Lett.*, *29*(11), 1535, doi:10.1029/2001GL013842.
Cully, C. M., et al. (2008), The THEMIS digital fields board, *Space Sci. Rev.*, *141*, 343–355, doi:10.1007/s11214-008-9417-1.
Evans, J. (1969), Theory and practice of ionospheric study by Thomson scatter radar, *Proc. IEEE*, *57*, 496–530, doi:10.1109/PROC.1969.7005.
Galand, M., R. G. Roble, and D. Lummerzheim (1999), Ionization by energetic protons in Thermosphere-Ionosphere Electrodynamics General Circulation Model, *J. Geophys. Res.*, *104*, 27,973–27,989, doi:10.1029/1999JA900374.
Henderson, M. G., G. D. Reeves, and J. S. Murphree (1998), Are north–south aligned auroral structures an ionospheric manifestation of bursty bulk flows?, *Geophys. Res. Lett.*, *25*, 3737–3740, doi:10.1029/98GL02692.
Jackel, B. J., F. Creutzberg, E. F. Donovan, and L. L. Cogger (2003), Triangulation of auroral red-line emission heights, *Sodankylä Geophys. Obs. Publ.*, *92*, 97–100.
Kauristie, K., V. A. Sergeev, O. Amm, M. V. Kubyshkina, J. Jussila, E. Donovan, and K. Liou (2003), Bursty bulk flow intrusion to the inner plasma sheet as inferred from auroral observations, *J. Geophys. Res.*, *108*(A1), 1040, doi:10.1029/2002JA009371.

Kennel, C. F., and F. Engelmann (1966), Velocity space diffusion from plasma turbulence in a magnetic field, *Phys. Fluids*, 9, 2377–2388, doi:10.1063/1.1761629.

Kennel, C. F., and H. E. Petschek (1966), Limit on stably trapped particle fluxes, *J. Geophys. Res.*, 71, 1–28.

Kennel, C. F., F. V. Scarf, and R. W. Fredricks (1970), VLF electric field observations in the magnetosphere, *J. Geophys. Res.*, 75, 6136–6152, doi:10.1029/JA075i031p06136.

Kepko, L., M. G. Kivelson, R. L. McPherron, and H. E. Spence (2004), Relative timing of substorm onset phenomena, *J. Geophys. Res.*, 109, A04203, doi:10.1029/2003JA010285.

Kepko, L., E. Spanswick, V. Angelopoulos, E. Donovan, J. McFadden, K.-H. Glassmeier, J. Raeder, and H. J. Singer (2009), Equatorward moving auroral signatures of a flow burst observed prior to auroral onset, *Geophys. Res. Lett.*, 36, L24104, doi:10.1029/2009GL041476.

Knight, S. (1973), Parallel electric field, *Planet. Space Sci.*, 21, 741–750, doi:10.1016/0032-0633(73)90093-7.

Liu, W., B.-L. Xu, J. Samson, and G. Rostoker (1995), Theory and observation of auroral substorms: A magnetohydrodynamic approach, *J. Geophys. Res.*, 100, 79–95.

Liu, W. W., et al. (2008), Observation of isolated high-speed auroral streamers and their interpretation as optical signatures of Alfvén waves generated by bursty bulk flows, *Geophys. Res. Lett.*, 35, L04104, doi:10.1029/2007GL032722.

Lui, A. T. Y., E. Spanswick, E. F. Donovan, J. Liang, W. W. Liu, O. LeContel, and Q.-G. Zong (2010), A transient narrow poleward extrusion from the diffuse aurora and the concurrent magnetotail activity, *J. Geophys. Res.*, 115, A10210, doi:10.1029/2010JA015449.

Lummerzheim, D., and J. Lilensten (1994), Electron transport and energy degradation in the ionosphere: Evaluation of the numerical solution, comparison with laboratory experiments and auroral observations, *Ann. Geophys.*, 12, 1039–1051.

Lummerzheim, D., M. Galand, J. Semeter, M. Mendillo, M. Rees, and F. Rich (2001), Emission of OI(630 nm) in proton aurora, *J. Geophys. Res.*, 106, 141–148, doi:10.1029/2000JA002005.

Lyons, L. R., T. Nagai, G. T. Blanchard, J. C. Samson, T. Yamamoto, T. Mukai, A. Nishida, and S. Kokubun (1999), Association between Geotail plasma flows and auroral poleward boundary intensifications observed by CANOPUS photometers, *J. Geophys. Res.*, 104, 4485–4500, doi:10.1029/1998JA900140.

Lyons, L. R., E. Zesta, Y. Xu, E. R. Sánchez, J. C. Samson, G. D. Reeves, J. M. Ruohoniemi, and J. B. Sigwarth (2002), Auroral poleward boundary intensifications and tail bursty flows: A manifestation of a large-scale ULF oscillation?, *J. Geophys. Res.*, 107(A11), 1352, doi:10.1029/2001JA000242.

Lyons, L. R., Y. Nishimura, Y. Shi, S. Zou, H.-J. Kim, V. Angelopoulos, C. Heinselman, M. J. Nicolls, and K.-H. Fornacon (2010), Substorm triggering by new plasma intrusion: Incoherent scatter radar observations, *J. Geophys. Res.*, 115, A07223, doi:10.1029/2009JA015168.

Lysak, R. L., and Y. Song (2000), The role of Alfvén waves in the formations of parallel electric fields, in *Magnetospheric Current Systems*, *Geophys. Monogr. Ser.*, vol. 118, edited by S. Ohtani et al., pp. 147–155, AGU, Washington, D. C.

Mälkki, A., A. Eriksson, P.-O. Dovner, R. Boström, B. Holback, G. Holmgren, and H. Koskinen (1993), A statistical survey of auroral solitary waves and weak double layers: 1. Occurrence and net voltage, *J. Geophys. Res.*, 98, 15,521–15,530, doi:10.1029/93JA01312.

McFadden, J. P., C. W. Carlson, D. Larson, V. Angelopoulos, M. Ludlam, R. Abiad, B. Elliott, P. Turin, and M. Marckwordt (2008), The THEMIS ESA plasma instrument and in-flight calibration, *Space Sci. Rev.*, 141, 277–302, doi:10.1007/s11214-008-9440-2.

Meier, R., D. Strickland, J. Hecht, and A. Christensen (1989), Deducing composition and incident electron spectra from ground-based auroral optical measurements: A study of auroral red line processes, *J. Geophys. Res.*, 94, 13,541–13,552, doi:10.1029/JA094iA10p13541.

Mende, S. B., et al. (2008), The THEMIS array of ground-based observatories for the study of auroral substorms, *Space Sci. Rev.*, 141, 357–387, doi:10.1007/s11214-008-9380-x.

Miyashita, Y., S. Machida, T. Mukai, Y. Saito, K. Tsuruda, H. Hayakawa, and P. R. Sutcliffe (2000), A statistical study of variations in the near and middistant magnetotail associated with substorm onsets: Geotail observations, *J. Geophys. Res.*, 105, 15,913–15,930, doi:10.1029/1999JA000392.

Mozer, F. S., and C. A. Kletzing (1998), Direct observation of large, quasi-static, parallel electric fields in the auroral acceleration region, *Geophys. Res. Lett.*, 25, 1629–1632, doi:10.1029/98GL00849.

Nakamura, R., L. F. Bargatze, T. Mukai, T. Nagai, K. B. Baker, M. R. Hairston, P. H. Reiff, A. A. Petrukovich, M. Nozdrachev, and O. A. Troshichev (1999), Response of the midtail electric field to enhanced solar wind energy input, *J. Geophys. Res.*, 104, 17,299–17,310, doi:10.1029/1999JA900166.

Nakamura, R., W. Baumjohann, M. Brittnacher, V. A. Sergeev, M. Kubyshkina, T. Mukai, and K. Liou (2001), Flow bursts and auroral activations: Onset timing and foot point location, *J. Geophys. Res.*, 106, 10,777–10,789, doi:10.1029/2000JA000249.

Nakamura, R., et al. (2004), Spatial scale of high-speed flows in the plasma sheet observed by Cluster, *Geophys. Res. Lett.*, 31, L09804, doi:10.1029/2004GL019558.

Ni, B., R. M. Thorne, R. B. Horne, N. P. Meredith, Y. Y. Shprits, L. Chen, and W. Li (2011), Resonant scattering of plasma sheet electrons leading to diffuse auroral precipitation: 1. Evaluation for electrostatic electron cyclotron harmonic waves, *J. Geophys. Res.*, 116, A04218, doi:10.1029/2010JA016232.

Nishimura, Y., L. Lyons, S. Zou, V. Angelopoulos, and S. Mende (2010), Substorm triggering by new plasma intrusion: THEMIS all-sky imager observations, *J. Geophys. Res.*, 115, A07222, doi:10.1029/2009JA015166.

Panov, E., et al. (2010), Multiple overshoot and rebound of a bursty bulk flow, *Geophys. Res. Lett.*, 37, L08103, doi:10.1029/2009GL041971.

Ponyavin, D. I., M. I. Pudovkin, and S. S. Sazhin (1977), Self-consistent field-aligned electric field in the Earth's magnetosphere, *Geomagn. Aeron.*, 17, 323–325.

Rees, M. (1989), *Physics and Chemistry of the Upper Atmosphere*, Cambridge Univ. Press, New York.

Rees, M., and D. Luckey (1974), Auroral electron energy derived from ratio of spectroscopic emissions: 1. Model computations, *J. Geophys. Res.*, 79, 5181–5186, doi:10.1029/JA079i034p05181.

Semeter, J., and F. Kamalabadi (2005), Determination of primary electron spectra from incoherent scatter radar measurements of the auroral E region, *Radio Sci.*, 40, RS2006, doi:10.1029/2004RS003042.

Semeter, J., C. Heinselman, G. G. Sivjee, H. U. Frey, and J. W. Bonnell (2005), Ionospheric response to wave-accelerated electrons at the poleward auroral boundary, *J. Geophys. Res.*, 110, A11310, doi:10.1029/2005JA011226.

Sergeev, V. A., K. Liou, P. T. Newell, S.-I. Ohtani, M. R. Hairston, and F. Rich (2004), Auroral streamers: Characteristics of associated precipitation, convection and field-aligned currents, *Ann. Geophys.*, 22, 537–548, doi:10.5194/angeo-22-537-2004.

Sergeev, V. A., T. A. Kornilova, I. A. Kornilov, V. Angelopoulos, M. V. Kubyshkina, M. Fillingim, R. Nakamura, J. P. McFadden, and D. Larson (2010), Auroral signatures of the plasma injection and dipolarization in the inner magnetosphere, *J. Geophys. Res.*, 115, A02202, doi:10.1029/2009JA014522.

Spanswick, E., E. F. Donovan, A. T. Y. Lui, E. L. Kepko, J. Liang, and W. Liu (2009), Motion of auroral features and plasma sheet flow, *Eos Trans. AGU*, 90(52), Fall Meet. Suppl., Abstract SM53D-06.

Steele, D., and D. McEwen (1990), Electron auroral excitation efficiencies and intensity ratios, *J. Geophys. Res.*, 95, 10,321–10,336, doi:10.1029/JA095iA07p10321.

Tripathi, A. K., and R. P. Singhal (2009), Diffusion coefficients from resonant interactions with electrostatic electron cyclotron harmonic waves, *Phys. Plasmas*, 16, 112107, doi:10.1063/1.3264735.

Vörös, Z., W. Baumjohann, R. Nakamura, M. Volwerk, and A. Runov (2006), Bursty bulk flow driven turbulence in the Earth's plasma sheet, *Space Sci. Rev.*, 122, 301–311, doi:10.1007/s11214-006-6987-7.

Waldteufel, P. (1971), On the analysis of high latitude incoherent scatter radar, *Rep. AO 30*, Arecibo Obs., Arecibo, P. R.

Xing, X., L. R. Lyons, V. Angelopoulos, D. Larson, J. McFadden, C. Carlson, A. Runov, and U. Auster (2009), Azimuthal plasma pressure gradient in quiet time plasma sheet, *Geophys. Res. Lett.*, 36, L14105, doi:10.1029/2009GL038881.

Zesta, E., L. R. Lyons, and E. Donovan (2000), The auroral signature of earthward flow bursts observed in the magnetotail, *Geophys. Res. Lett.*, 27, 3241–3244, doi:10.1029/2000GL000027.

Zesta, E., E. Donovan, L. Lyons, G. Enno, J. S. Murphree, and L. Cogger (2002), Two-dimensional structure of auroral poleward boundary intensifications, *J. Geophys. Res.*, 107(A11), 1350, doi:10.1029/2001JA000260.

Zesta, E., L. Lyons, C.-P. Wang, E. Donovan, H. Frey, and T. Nagai (2006), Auroral poleward boundary intensifications (PBIs): Their two-dimensional structure and associated dynamics in the plasma sheet, *J. Geophys. Res.*, 111, A05201, doi:10.1029/2004JA010640.

Zou, S., L. R. Lyons, M. J. Nicolls, and C. J. Heinselman (2008), PFISR observations of strong azimuthal flow bursts in the ionosphere and their relation to nightside aurora, *J. Atmos. Sol. Terr. Phys.*, 71, 729–737, doi:10.1016/j.jastp.2008.06.015.

Zou, S., L. R. Lyons, M. J. Nicolls, C. J. Heinselman, and S. B. Mende (2009), Nightside ionospheric electrodynamics associated with sub-

storms: PFISR and THEMIS ASI observations, *J. Geophys. Res.*, *114*, A12301, doi:10.1029/2009JA014259.

E. F. Donovan, J. Liang, and E. Spanswick, Department of Physics and Astronomy, University of Calgary, Calgary, AB T2N 1N4, Canada. (jliang@phys.ucalgary.ca)

W. W. Liu, Space Science, Canadian Space Agency, 6767 Route de l'Aeroport, Saint-Hubert, QC J3Y 8Y9, Canada.

D. Lummerzheim, Geophysical Institute, University of Alaska Fairbanks, Fairbanks, AK 99775, USA.

M. J. Nicolls, SRI International, 333 Ravenswood Ave., Menlo Park, CA 94025, USA.